N71-28007

NASA TECHNICAL NOTE

NASA TN D-6281

NASA TN D-6281

CASE FILE COPY

FLOW PATTERNS AND PRESSURE DISTRIBUTIONS AROUND A BLUFF AFTERBODY IN THE WAKE OF A 120° CONE FOR VARIOUS SEPARATION DISTANCES AT MACH 3.0

by William D. Deveikis and James Wayne Sawyer

Langley Research Center
Hampton, Va. 23365

NATIONAL AERONAUTICS AND SPACE ADMINISTRATION • WASHINGTON, D. C. • JUNE 1971

1. Report No.	2. Government Accession No.	3. Recipient's Catalog No.
NASA TN D-6281		

4. Title and Subtitle	5. Report Date
FLOW PATTERNS AND PRESSURE DISTRIBUTIONS AROUND A BLUFF AFTERBODY IN THE WAKE OF A 120° CONE FOR VARIOUS SEPARATION DISTANCES AT MACH 3.0	June 1971
	6. Performing Organization Code
7. Author(s)	8. Performing Organization Report No.
William D. Deveikis and James Wayne Sawyer	L-7542
	10. Work Unit No.
9. Performing Organization Name and Address	124-07-23-01
NASA Langley Research Center Hampton, Va. 23365	11. Contract or Grant No.
	13. Type of Report and Period Covered
12. Sponsoring Agency Name and Address	Technical Note
National Aeronautics and Space Administration Washington, D.C. 20546	14. Sponsoring Agency Code

15. Supplementary Notes

16. Abstract

A wind-tunnel investigation of an attached inflatable decelerator concept was conducted at a Mach number of 3.0 with solid models to observe the effects of varying the separation distance between the 120° cone forebody and the inflated afterbody shape on flow patterns and pressure distributions. Flow-visualization tests were conducted for separation distances up to 4.74 forebody diameters and at free-stream Reynolds numbers, based on afterbody maximum diameter, between 0.57×10^6 and 3.20×10^6. Pressure-distribution tests were conducted for separation distances up to 2.49 forebody diameters at free-stream Reynolds numbers, based on afterbody maximum diameter, between 10.0×10^6 and 11.8×10^6. The afterbody was constructed with a burble fence so that the afterbody-to-forebody frontal area ratio was 6.2.

17. Key Words (Suggested by Author(s))	18. Distribution Statement
Attached inflatable decelerator Cones Wake Pressure distributions, Flow patterns	Unclassified – Unlimited

19. Security Classif. (of this report)	20. Security Classif. (of this page)	21. No. of Pages	22. Price*
Unclassified	Unclassified	42	$3.00

*For sale by the National Technical Information Service, Springfield, Virginia 22151

FLOW PATTERNS AND PRESSURE DISTRIBUTIONS AROUND A BLUFF AFTERBODY IN THE WAKE OF A 120° CONE FOR VARIOUS SEPARATION DISTANCES AT MACH 3.0

By William D. Deveikis and James Wayne Sawyer
Langley Research Center

SUMMARY

A wind-tunnel investigation of an attached inflatable decelerator concept was conducted at a Mach number of 3.0 with solid models to observe the effects of varying the separation distance between the 120° cone forebody and the inflated afterbody shape on flow patterns and pressure distributions. Of interest was the influence of the bluff forebody wake on the afterbody to aid in determining the feasibility of using the inflated afterbody to extricate a payload from the forebody while traveling supersonically. Flow-visualization tests were conducted for separation distances up to 4.74 forebody diameters and at free-stream Reynolds numbers, based on afterbody maximum diameter, between 0.57×10^6 and 3.2×10^6. Pressure-distribution tests were conducted for separation distances up to 2.49 forebody diameters at free-stream Reynolds numbers, based on afterbody maximum diameter, between 10.0×10^6 and 11.8×10^6. The afterbody was constructed with a burble fence so that the afterbody-to-forebody frontal area ratio was 6.2.

The flow-visualization tests revealed specific ranges of separation distance for which the cone forebody wake was either divergent or convergent. There was also an intermediate range of separation distances in which both types of configuration were obtainable. The pressure-distribution test results indicated that, as the separation distance for divergent wakes increased, the negative pressure gradient along the cone became stronger; the cone wake pressures decreased; the afterbody front surface area within the cone wake increased; afterbody ram and surface pressures within the cone wake decreased to wake pressure; and the drag coefficients of the cone and afterbody increased and decreased, respectively. Using drag coefficients evaluated from the surface-pressure distributions, computations of the acceleration of each body over a range of the afterbody-to-forebody mass ratio from 0 to 6.2 indicated that unlimited separation of the two bodies will occur only for afterbody-to-forebody mass ratios less than approximately 1.55.

INTRODUCTION

As discussed in reference 1, the attached inflatable decelerator concept illustrated in figure 1 is very efficient in terms of its low structural weight and the drag that can be developed. Consequently, one of the uses envisioned for it is on unmanned atmospheric entry systems designed to deliver a payload to the surface of a planet. The payload and inflatable afterbody are packaged behind the large-angle cone forebody which serves both as a heat shield and as a decelerator on entry. During the entry phase the inflatable afterbody is deployed supersonically to augment the drag of the forebody and thus assist in making a soft landing.

For some missions, it may be desirable to jettison the forebody prior to touchdown, in which case the inflatable afterbody might also serve to assist in extricating the payload. Conceivably, mission requirements may also dictate that the forebody be jettisoned while the decelerator is traveling at supersonic speed. Although several techniques for supersonic deployment of the inflatable afterbody have been successfully demonstrated in wind-tunnel tests as reported in references 2, 3, and 4, experimental information is lacking on the behavior of the two bodies during their separation. Thus, the present investigation was conducted to study the flow field and mutual interference of the two bodies at varying separation distances for a Mach number of 3.0.

A sting-mounted pressure-distribution model was tested in the Langley 9- by 6-foot thermal structures tunnel to determine the effects of forebody wake on afterbody ram and surface pressures for separation distances up to 2.49 forebody diameters. In addition, flow-visualization tests were conducted in the Langley 9- by 6-inch model tunnel using a 1/16-scale model of the pressure-distribution model for separation distances up to 4.74 forebody diameters. Free-stream Reynolds number, based on afterbody maximum diameter, was nominally 11.5×10^6 for the pressure-distribution tests and varied between 0.57×10^6 and 3.2×10^6 for the flow-visualization tests. With the burble fence included, the afterbody-to-forebody frontal area ratio was 6.2.

SYMBOLS

Although physical quantities were measured in U.S. Customary Units, they are presented in this paper in the International System of Units (SI). Factors relating the two systems are given in reference 5.

C_D drag coefficient, $2\int_0^1 C_{p,f}\left(\frac{r}{r_{ref}}\right)d\left(\frac{r}{r_{ref}}\right) - 2\int_0^1 C_{p,b}\left(\frac{r}{r_{ref}}\right)d\left(\frac{r}{r_{ref}}\right)$

C_p surface pressure coefficient, $\frac{p_l - p}{q}$

$C_{p,f}$	surface pressure coefficient on front surface
$C_{p,b}$	surface pressure coefficient on back surface
d_c	cone diameter
l_c	cone length
M_l	local Mach number
m_a	mass of afterbody
m_c	mass of cone
p	free-stream static pressure
p_l	local surface pressure
p_r	ram pressure
q	free-stream dynamic pressure
r	radial coordinate (fig. 2)
r_b	maximum radius of afterbody (fig. 2)
r'_b	maximum radius of burble fence (fig. 2)
r_c	base radius of cone (fig. 2)
r_n	radius of spherical nose
r_{ref}	maximum reference radius $(r_b,\ r'_b,$ or $r_c)$
x	axial coordinate (fig. 2)
δ	separation distance between cone and afterbody (fig. 2)

MODELS, APPARATUS, AND TESTS

Models

Sketches of the flow-visualization and the pressure-distribution models are shown in figure 2. For both models, the forebody was a spherically blunted $\left(r_n/r_b \approx 0.12\right)$ 120° cone with a flat shoulder at the cone base rim. On the flow-visualization model, this shoulder was oriented parallel with the cone axis, whereas on the pressure-distribution model, the shoulder was machined normal to the cone front surface. The afterbody was constructed with a burble fence whose leading edge was $0.045r_b$ upstream of the circle generated by the afterbody maximum radius r_b. The maximum radius of the burble fence was $1.10r_b$ and provided a total projected frontal area 6.2 times that of the forebody. On the flow-visualization model, the rear surface was machined flat at the cone and afterbody base, whereas on the pressure-distribution model, the cone forebody was machined as a shell, and its afterbody was constructed with the base cavity. A sting whose diameter was 0.14 times that of the cone base diameter was used to vary the separation distance between the bodies.

The flow-visualization model and the cone forebody of the pressure-distribution model were constructed of stainless steel with surfaces polished to a finish of approximately 254 nm, rms. The afterbody of the pressure-distribution model was constructed of cherry wood. Its surface was impregnated with epoxy resin and then polished. The afterbodies for both models were machined without the lobing shown in figure 1. Model coordinates are given in table I.

Static- and ram-pressure orifices were installed in the pressure-distribution model at the locations indicated in figure 2(b) and table II. Static pressures were measured at 10 stations along the outer surface and at 7 stations along the inner surface of the cone forebody and at 53 stations along the afterbody and burble fence. These orifices were located in a plane containing the model axis. Ram pressures were measured at six stations along the afterbody at a distance 0.64 cm above the surface. These orifices were staggered circumferentially to avoid mutual interference.

Model-sting-mount configurations for the flow-visualization and the pressure-distribution tests are illustrated in figure 3. The flow-visualization model was supported by a pistol-grip sting mount, whereas the pressure-distribution model was supported by a cruciform sting mount that was located approximately 3 afterbody maximum diameters downstream of the model base.

Instrumentation

Shock waves and flow patterns generated by the flow-visualization model were recorded photographically with the aid of a single-path horizontal Z-light-path schlieren

system and a spark light source of approximately 0.2-microsecond duration. Pressures were measured with the aid of strain-gage pressure transducers connected to orifice tubes in the pressure-distribution model. The output from the transducers was recorded and reduced to useful form at the Langley central digital data recording facility. Based on a deflection of 1 percent of full scale, the values of the pressure coefficients determined from the transducer data are estimated to be accurate within 0.025.

Test Facilities

The flow-visualization model was tested in the Langley 9- by 6-inch model tunnel, whereas the pressure-distribution model was tested in the Langley 9- by 6-foot thermal structures tunnel. Both facilities are blowdown wind tunnels which operate at a Mach number of 3.0 with less than 1 percent deviation. The 9- by 6-inch model tunnel is equipped with an air ejector that permits it to operate at stagnation pressures between 269 and 1380 kN/m^2 absolute. The 9- by 6-foot thermal structures tunnel operates at stagnation pressures between 345 and 1380 kN/m^2 absolute. Both facilities can operate over a stagnation-temperature range between ambient and 1360 K and use the same air supply. Other details on these facilities may be found in reference 6.

Tests

All tests were conducted with the model oriented at 0° incidence with respect to the tunnel longitudinal center line. The flow-visualization tests were conducted at ambient stagnation temperatures for increments of the separation distance as small as $0.018d_c$ and for separation distances up to $4.74d_c$. At each separation distance, flow patterns were observed throughout the stagnation-pressure range of the facility, and representative schlieren photographs were taken. Free-stream Reynolds number, based on afterbody maximum diameter $2r_b$, varied between 0.57×10^6 and 3.20×10^6. To obtain schlieren photographs of the flow patterns at small separation distances, the front face of the afterbody was cut back to match the flat surface of the cone forebody base. Hence, two afterbody shapes are shown in the schlieren photographs reproduced herein. For these tests, the tunnel was operated for as long as 10 minutes.

The pressure-distribution tests were conducted over a range of 10 separation distances up to $2.49d_c$. The afterbody was also tested without the cone forebody to simulate conditions at very large separation distances. For this case, a 130° cone tip was added to the afterbody to cover the flat surface that was exposed on removing the cone forebody. Stagnation temperature was constant for each test but varied between 350 K and 392 K over this series of tests. Thus, the free-stream Reynolds number, based on afterbody maximum diameter $2r_b$ varied between 10.0×10^6 and 11.8×10^6. Test duration was approximately 30 seconds to provide sufficient time for pressures sensed by the transducers to reach equilibrium.

RESULTS AND DISCUSSION

Flow Patterns

Schlieren photographs taken during the flow-visualization tests revealed distinctive flow patterns at different separation distances. Typical features are illustrated and identified in figure 4. When the cone forebody and the afterbody were unseparated, the resulting flow pattern, shown in figure 4(a), was generally characteristic of patterns that were observed in the investigation of reference 3 on other attached inflatable decelerator shapes. However, the boundary-layer flow separation from the cone rim and its subsequent reattachment onto the afterbody were unique for the present decelerator shape because the shapes of reference 3 had no rearward-facing step at the cone juncture with the afterbody.

At values of $\frac{\delta}{d_c} > 0$, the flow features differed primarily by the cone wake configuration – that is, whether it diverged as in figure 4(b) or converged as in figure 4(c). For the flow pattern illustrated in figure 4(b), the presence of the afterbody restricted the expansion of the flow around the cone rim so that the separated shear layer spanned the distance between the bodies as shown. Thus, the shaded space between the bodies comprised a separated-flow region wherein the flow circulated as indicated. The resulting forebody-wake-afterbody configuration appears to operate as a single body in which the wake serves as a truncated conical center section. This flow pattern is believed to be free of forebody sting effects and, therefore, representative of free flight.

For the flow pattern illustrated in figure 4(c), the afterbody did not restrict the expansion of flow around the cone rim. Hence, the flow was able to converge behind the cone and form a narrow, viscous wake in a manner characteristic of a natural wake behind a bluff body as shown in the schlieren photograph of the cone forebody in figure 5. However, the presence of the afterbody forced the flow to separate from the sting at a location well ahead of the afterbody. This effect is consistent with similar effects observed in other investigations such as those reported in references 7 and 8 on blunt axisymmetric bodies with spikes. Thus, in the present tests, the afterbody would have encountered flow separation effects regardless of the sting length, and in this respect, the flow pattern of figure 4(c) differs from that which would be obtained in free flight. In free flight, the afterbody would experience some effects from the narrow, viscous wake but such effects would become negligible at sufficiently large separation distances, and attached flow would be expected thereafter.

Schlieren photographs of the flow details around the bodies at various separation distances are shown in figure 6. Figure 6(a) shows a photograph of the flow pattern taken when $\frac{\delta}{d_c} = 0$ and was used in preparing figure 4(a). In the present investigation,

the divergent and convergent cone wake configurations occurred for ranges of separation distances that were independent of Reynolds number over the operating range of the test facility. Thus, for separation distances up to $\frac{\delta}{d_c} = 3.75$, the cone wake always diverged as in figures 6(b) to 6(j), whereas for $\frac{\delta}{d_c} > 4.60$, the cone wake always converged as in figure 6(m). The separation distances between $3.75 < \frac{\delta}{d_c} < 4.60$ comprised an intermediate range wherein both cone wake configurations were obtainable at a given separation distance as in figures 6(k) and 6(ℓ). The existence of an intermediate range of separation distances became evident during one of the tests when a divergent wake that had persisted throughout the tunnel operating pressure range suddenly collapsed into a convergent wake after the pressure had decreased to a level near the unstarting pressure. The convergent wake then persisted throughout the tunnel pressure range. This effect also occurred at higher pressures, but once a divergent wake collapsed, it could not be made to diverge again. The factors involved in collapsing the divergent wake are not known. Temperature, which affects boundary-layer characteristics, should not have been a factor because the tunnel was operated at sufficiently long periods of time for the model temperature to have stabilized.

Within the range of separation distances for divergent cone wakes, the bluffness of the bow shock wave, the shock standoff distance ahead of the cone, and the wake angle decreased as the wake elongated with increasing separation distance. Simultaneously, the cone wake masked an increasing amount of afterbody front surface so that at a separation distance of only $\frac{\delta}{d_c} = 0.56$ (fig. 6(f)), virtually all of the afterbody front surface was immersed in the cone wake. In the range of separation distances for convergent cone wakes, no effect of separation distance on cone wake geometry was observed. However, the presence of the cone sting may have influenced the location of the cone wake neck.

Pressure Distribution

Zero separation distance.- The pressure-distribution model was tested both with and without the burble fence when the forebody and afterbody were unseparated. The model without the burble fence was tested primarily to provide reference data. Ram and surface pressures from these two configurations yielded the local Mach numbers given in figure 7 as determined from the ratio of local static pressure to local total pressure. These results show that the local Mach numbers were approximately the same for both configurations. Thus, the flow characteristics were not affected by the presence of

the burble fence for values of $\frac{r}{r_b} < 0.90$. Sonic conditions occurred on the afterbody where the local radius was approximately $\frac{r}{r_b} = 0.81$.

Longitudinal ram- and surface-pressure coefficient distributions obtained at zero separation distance are presented in figure 8 for the model with and without the burble fence. Pressure data for these configurations are also given in tables I and II. The plotted data show that ram pressures upstream of the sonic point were about 3.5 percent higher than the stagnation-point pressure and, as indicated in table II, were nearly twice the free-stream dynamic pressure. On the model without the burble fence, the ram pressure obtained near the maximum diameter of the afterbody (fig. 8(a)) was substantially reduced by normal-shock losses resulting from the formation of a detached shock wave ahead of the orifice.

The surface-pressure data for both model configurations showed a negative gradient where the flow was attached and showed fairly uniform values at less than free-stream static pressure along the rear surface of the afterbody. Although the cone rim touched the afterbody at this separation distance, the space between the bodies was vented to the stream. Consequently, the data obtained along the cone back surface and along the afterbody front surface that was shielded by the cone indicated that the pressure within this space stabilized at a level to which the external flow expanded around the cone rim. The peak pressure on the afterbody just downstream of the cone rim indicates reattachment of the shear layer after its separation off the cone rim. The surface-pressure rise and peak shown near the burble fence in figure 8(b) is associated with boundary-layer flow separation from the afterbody surface and its subsequent reattachment on the front face of the burble fence.

With the exception of the region near the cone-afterbody juncture, these pressure distributions showed characteristics that were similar to those obtained on the attached inflatable decelerator model of reference 3 designated as shape 2. The sensitivity of the pressures in this region to surface perturbations is shown in figure 9, where pressures obtained from the reference model are compared with present values. As shown in the sketch at the top of the figure, the afterbody profiles of both models ahead of the burble fence were similar, but the reference model was constructed with a compression corner at the cone-afterbody juncture instead of a rearward-facing step as on the present model. Consequently, a less favorable pressure gradient resulted along the cone forebody of the reference model such that its value was nearly zero at the juncture.

Separation distances greater than zero.- For separation distances up to $\frac{\delta}{d_c} = 2.49$, the divergent cone wake affected the ram and surface pressures as shown in figures 10(a) to 10(i) and in tables I and II. From figure 10 it is observed that, along the cone front

surface, the negative pressure gradient became stronger with increasing separation distance up to $\frac{\delta}{d_c} = 0.23$ and remained relatively unchanged at the longer separation distances. The pressures along the cone back surface were fairly uniform at all separation distances but decreased with each extension since the volume enclosed by the cone wake shear layer increased. These observations correlate with those from figure 6 concerning the bow shock-wave shape, its standoff distance, and the decreasing cone wake angle. On the afterbody, a most significant observation was the devastating effect on ram- and surface-pressure distributions produced by the cone wake. The ram and surface pressures that were exposed to the wake environment collapsed to values as low as the cone base pressure, and each extension of the separation distance increased the area over which the pressures were affected. At a separation distance of $\frac{\delta}{d_c} = 0.11$ (fig. 10(c)), the ram pressures downstream of the peak surface pressure associated with wake shear layer reattachment began decreasing, and surface pressures in the separated flow region ahead of the burble fence began to change because of wake shear layer disturbances. At a separation distance of $\frac{\delta}{d_c} = 2.49$ (fig. 10(i)), all ram pressures showed static values, and surface pressures were depressed all along the front face of the burble fence which signified that the entire front face of the afterbody was engulfed by the cone wake. Consequently, a divergent cone wake would adversely affect the shape and aerodynamic performance of an inflatable afterbody by virtue of the large changes in loading it produces. At the separation distance $\frac{\delta}{d_c} = 2.49$, the surface pressures on the front end of the afterbody were only slightly higher than the afterbody base pressure. Presumably, a convergent cone wake would occur at a separation distance at which the cone base pressure and the afterbody base pressure become equal. No effect of separation distance on afterbody base pressure was observed.

Figure 10(j) shows the ram and surface pressures over the afterbody without the cone forebody. These pressures are considered representative of those obtained at very large separation distances free of any influence of the cone forebody wake. For this case, the flow along the front face of the afterbody is attached, and the ram and surface pressures are similar to those obtained at $\frac{\delta}{d_c} = 0$.

Influence of Mass Ratio on Body Separation Distance

The drag coefficients of the cone forebody and the afterbody were calculated at each separation distance by integrating the pressure-distribution curves of figures 8(b) and 10 and are presented in figure 11. The value given for the cone at the separation distance of infinity was taken from reference 9 and was adjusted to true cone base pressure. As shown, the drag coefficient of the cone forebody increased with increasing separation

distance, whereas effects of the divergent cone wake resulted in decreasing values of the afterbody drag coefficient. At larger separation distances where the cone wake converges, higher values of the afterbody drag coefficient would be expected such as indicated by the data point at $\frac{\delta}{d_c} = \infty$.

These drag coefficients were used in computing the acceleration of each body for values of afterbody-to-forebody mass ratio between 0 and 6.2. The results showed that at every separation distance, there exists a value of afterbody-to-forebody mass ratio at which the acceleration of both bodies will become equal, and, therefore, the bodies will not continue to separate. A locus of points defining the limiting distances to which the present bodies will separate is plotted in figure 12 as the variation of mass ratio with separation distance. The curve applies only for an afterbody-to-forebody area ratio of 6.2. Within the range of separation distances where the cone wake diverges, the limiting separation distance is very small at high values of the mass ratio and increases as the mass ratio is reduced. The trend of the curve suggests that there is a minimum value of mass ratio less than $m_a/m_c = 1.55$ below which the separation distance would be unlimited. A minimum value of mass ratio should occur at the separation distance at which the cone wake first converges since the drag of the afterbody would increase as effects of the divergent cone wake diminished. At sufficiently large separation distances where cone wake effects are negligible, the mass ratio for unlimited body separation increases to 4.36.

Admittedly, these results ignore the relative motion and other dynamic effects that might exist between the forebody and afterbody in actual flight since they are based on static test data. However, in view of the unrealistically low mass ratios that appear to be required for unlimited separation, it is doubtful that a payload can be extricated from the forebody by using the afterbody at supersonic speeds.

CONCLUSIONS

A wind-tunnel investigation of an attached inflatable decelerator concept was conducted at a Mach number of 3.0 with solid models to observe the effects of varying the separation distances between the 120° cone forebody and the inflated afterbody shape on flow patterns and pressure distributions. Attention was focused on the influence of the bluff forebody wake on the afterbody to aid in determining the feasibility of using the inflated afterbody to extricate a payload from the forebody. With burble fence included, the afterbody-to-forebody frontal area ratio was 6.2. The results, which did not account for dynamic effects, indicated the following conclusions:

1. There are specific ranges of body separation distances for which the cone forebody wake is either divergent or convergent. In addition, there is an intermediate range between 3.75 and 4.60 cone forebody diameters wherein both types of wake configurations are obtainable at a given separation distance.

2. A divergent wake will adversely affect the shape and aerodynamic performance on an inflatable afterbody by virtue of the large changes in loading it produces.

3. Computations of the accelerations of each body using drag coefficients from the experimental pressure distributions indicate that separation of the two bodies at Mach 3.0 appears feasible only for low values of afterbody-to-forebody mass ratio (less than 1.55).

Langley Research Center,
National Aeronautics and Space Administration,
Hampton, Va., April 28, 1971.

REFERENCES

1. Guy, L. D.: Structural and Decelerator Design Options for Mars Entry. J. Spacecraft Rockets, vol. 6, no. 1, Jan. 1969, pp. 44-49.

2. Mikulas, Martin M., Jr.; and Bohon, Herman L.: Development Status of Attached Inflatable Decelerators. J. Spacecraft Rockets, vol. 6, no. 6, June 1969, pp. 654-660.

3. Deveikis, William D.; and Sawyer, James Wayne: Static Aerodynamic Characteristics, Pressure Distributions, and Ram-Air Inflation of Attached Inflatable Decelerator Models at Mach 3.0. NASA TN D-5816, 1970.

4. Bohon, Herman L.; and Miserentino, R.: Deployment and Performance Characteristics of 5-Foot-Diameter (1.5 m) Attached Inflatable Decelerators From Mach Number 2.2 to 4.4. NASA TN D-5840, 1970.

5. Comm. on Metric Pract.: ASTM Metric Practice Guide. NBS Handbook 102, U.S. Dep. Com., Mar. 10, 1967.

6. Schaefer, William T., Jr.: Characteristics of Major Active Wind Tunnels at the Langley Research Center. NASA TM X-1130, 1965.

7. Jones, Jim J.: Experimental Drag Coefficients of Round Noses With Conical Windshields at Mach Number 2.72. NACA RM L55E10, 1955.

8. Crawford, Davis H.: Investigation of the Flow Over a Spiked-Nose Hemisphere-Cylinder at a Mach Number of 6.8. NASA TN D-118, 1959.

9. Deveikis, William D.; and Sawyer, James Wayne: Effects of Cone Angle, Base Flare Angle, and Corner Radius on Mach 3.0 Aerodynamic Characteristics of Large-Angle Cones. NASA TN D-5048, 1969.

TABLE I.- MODEL COORDINATES AND SURFACE PRESSURES

Surface	Orifice	$\frac{x}{r_b}$	$\frac{r}{r_b}$	C_p for δ/d_c of –											
				a_0	0	0.028	0.057	0.113	0.226	0.339	0.565	0.905	1.357	2.490	∞
Cone front face	1	0	0	1.758	1.753	1.765	1.760	1.763	1.753	1.758	1.758	1.754	1.760	1.757	
	2	.011	.050	1.722	1.713	1.718	1.705	1.696	1.677	1.683	1.695	1.678	1.692	1.698	
	3	.039	.100	1.691	1.686	1.684	1.668	1.653	1.631	1.634	1.644	1.633	1.643	1.654	
	4	.068	.150	1.653	1.637	1.651	1.632	1.696	1.596	1.596	1.604	1.590	1.595	1.620	
	5	.097	.200	1.636	1.6[illegible]	1.622	1.601	1.579	1.558	1.560	1.565	1.553	1 566	1.574	
	6	.125	.250	1.614	1.602	1.594	1.568	1.540	1.515	1.518	1.517	1.501	1.522	1.527	
	7	.154	.300	1.596	1.543	1.569	1.535	1.498	1.470	1.473	1.475	1.459	1.478	1.479	
	8	.183	.350	1.570	1.562	1.536	1.494	1.438	1.402	1.403	1.410	1.389	1.406	1.409	
	9	.212	.400												
	10	.232	.435	1.512	1.504	1.427	1.351	1.199	1.079	1.076	1.086	1.069	1.081	1.085	
Cone rear face	11	0.240	0.435												
	12	.223	.400	1.393	1.366	1.405	1.317	1.107	0.767	0.581	0.377	0.240	0.167	0.095	
	13	.199	.350	1.395	1.365	1.419	1.315	1.117	.771	.587	.388	.252			
	14	.174	.300	1.396	1.364	1.404	1.315	1.108	.769	.583	.380	.244	.172	.099	
	15	.150	.250	1.394	1.364	1.412	1.324	1.110	.763	.578	.377	.241	.168	.094	
	16	.126	.200	1.404	1.375	1.406	1.317	1.102	.753	.558	.351	.211	.141	.065	
	17	.102	.150	1.394	1.370										
Afterbody front face	18	0.007	0.150												1.673
	19	.018	.175	1.397	1.375	1.404	1.316	1.107	0.768	0.581	0.377	0.234	0.149	0.080	1.686
	20	.026	.201			1.408	1.320	1.107	.764	.576	.374	.224	.139	.071	1.686
	21	.037	.225	1.397	1.380	1.404	1.315	1.106	.768	.579	.375	.230	.145	.076	1.663
	22	.046	.250	1.400		1.406	1.316	1.107	.769	.580	.374	.230	.142	.070	1.668
	23	.057	.275	1.399	1.379	1.405	1.315	1.108	.769	.582	.376	.231	.145	.077	1.625
	24	.066	.301	1.406		1.408	1.313	1.104	.750	.559	.348	.199	.108	.044	1.609
	25	.073	.326	1.403	1.379	1.405	1.315	1.107	.768	.580	.370	.225	.134	.068	1.611
	26	.087	.350	1.398		1.405	1.316	1.105	.764	.573	.365	.215	.156	.058	1.515
	27	.100	.376												
	28	.109	.401	1.378	1.355	1.403	1.313	1.106	.769	.582	.399	.257	.194	.135	1.557
	29	.122	.426	1.382	1.364	1.403	1.313	1.104	.765	.576	.370	.220	.130	.062	1.524
	30	.124	.434	1.355	1.330	1.401	1.312	1.101	.759	.568	.362	.207	.127	.053	1.515
	31	.136	.460	1.647	1.643	1.393	1.312	1.091	.733	.534	.329	.178	.110	.049	1.522
	32	.156	.500	1.530	1.526	1.482	1.291	1.088	.759	.550	.371	.193	.135	.049	1.489
	33	.187	.563	1.441	1.434	1.514	1.499	1.088	.730	.539	.327	.189	.121	.055	1.421
	34	.220	.623	1.301	1.326	1.369	1.445	1.247	.747	.543	.342	.210	.176	.108	1.314
	35	.222	.627	1.339	1.322	1.372	1.427	1.200	.743	.548	.346	.211	.176	.080	1.316
	36	.251	.676		1.210	1.250	1.309	1.380	.878	.603	.373	.214	.188	.118	1.202
	37	.285	.725	1.166	1.158	1.186	1.220	1.323	1.063	.787	.514	.334	.307	.208	1.160
	38	.320	.772	1.032	1.026	1.050	1.076	1.187	1.107	.911	.646	.448	.384	.266	1.032
	39	.323	.775	1.013	.998	1.026	1.052	1.148	1.059	.863	.597	.398	.361	.186	1.000
	40	.357	.815	.903	.884	.893	.916	1.022	1.022	.935	.745	.559	.451	.314	.876
	41	.398	.857	.757	.757	.774	.790	.877	.899	.866	.755	.618	.499	.365	.765
	42	.443	.895	.601	.598	.609	.620	.691	.723	.713	.657	.581	.478	.379	.600
	43	.502	.934	.385	.390	.397	.402	.449	.491	.497	.476	.441	.377	.341	.406
	44	.505	.937	.363	.356	.374	.375	.420	.442	.441	.414	.378	.332	.306	.368
	45	.580	.970	.185	.340	.344	.338	.291	.371	.377	.363	.349	.396	.377	.363
	46	.624	.984	.108	.474	.478	.478	.508	.566	.580	.570	.546	.517	.455	.477
	47	.693	.997	.021		.473	.473	.501	.566	.590	.595	.522	.559	.506	.470
	48	.767	1.000	-.041											
Burble fence	49	0.727	1.012		0.448	0.453	0.462	0.503	0.569	0.596	0.622	0.614	0.598	0.543	0.445
	50	.733	1.032			.427	.345	.568	.652	.695	.702	.707	.685	.627	.502
	51	.741	1.050		.624	.629	.639	.694	.766	.776	.756	.728	.686	.593	.629
	52	.758	1.073		.629	.634	.631	.639	.651	.633	.596	.554	.492	.423	.633
	53	.778	1.087		.350	.356	.351	.347	.359	.350	.332	.305	.262	.223	.348
	54	.799	1.095		.106	.103	.100	.099	.112	.110	.108	.094	.087	.077	.099
	55	.833	1.099		-.036	-.032	-.036	-.035	-.027	.023	-.026	-.029	-.036	-.040	-.040
	56	.864	1.090		-.069	-.057	-.066	-.072	-.085	-.084	-.083	-.080	-.084	-.093	-.069
	57	.888	1.070		-.070	-.062	-.102	-.056	-.071	-.110	-.109	-.096	-.106	-.105	-.095
	58	.900	1.030		-.097	-.054	-.064	-.072	-.073	-.081	-.081	-.077	-.083	-.092	-.068
	59	.890	1.000		-.082	-.120	-.109	-.085	-.072		-.106	-.141	-.042	-.100	
Afterbody rear face	60	0.822	0.991	-0.087											
	61	.874	.972	-.083	-0.079	-0.073	-0.078	-0.085	-0.096	-0.096	-0.097	-0.095	-0.090	-0.095	-0.079
	62	.933	.934	-.092	-.072	-.081	-.086	-.093	-.104	-.104	-.104	-.065	-.104	-.109	-.086
	63	.973	.895												
	64	.999	.856	-.075	-.077	-.069	-.075	-.083	-.095	-.095	-.094	-.093	-.099	-.105	-.079
	65	1.035	.772	-.086	-.072	-.078	-.085	-.096	-.107	-.107	-.109	-.107	-.109	-.115	-.090
	66	1.047	.675	-.085	-.069	-.068	-.072	-.090	-.103	-.103	-.109	-.107	-.106	-.114	-.086
	67	1.027	.565	-.066	-.051	.008	-.014	-.035	-.050	-.057	-.095	-.092	-.058	-.049	-.095
	68	.955	.425	-.060	-.060										
	69	.821	.300	-.077	-.075	-.073	-.074	-.075	-.082	-.080	-.080	-.079	-.079	-.082	-.074
	70	.694	.225	-.015	-.004	.011	-.003	-.010	-.023	-.012	-.005	-.012	-.009	-.010	-.012

[a]Without burble fence.

TABLE II.- RAM PRESSURES

Ram orifice	$\frac{x}{r_b}$	$\frac{r}{r_b}$	p_r/q for δ/d_c of –											
			a_0	0	0.028	0.057	0.113	0.226	0.339	0.565	0.905	1.357	2.490	∞
1	0.129	0.505	1.972	1.963	1.952	1.466	1.252	0.917	0.725	0.513	0.358	0.261	0.193	1.802
2	.183	.608	1.965	1.953	1.975	1.945	1.324	.871	.688	.484	.339	.263	.205	1.794
3	.245	.714	1.972	1.953	1.986	1.974	1.863	1.162	.785	.510	.359	.315	.255	1.793
4	.322	.812	1.989	1.981	1.998	1.990	1.934	1.638	1.303	.877	.590	.517	.378	1.795
5	.442	.926	1.945	1.934	1.960	1.948	1.912	1.748	1.643	1.381	1.084	.944	.564	1.772
6	.730	1.025	1.215											

[a]Without burble fence.

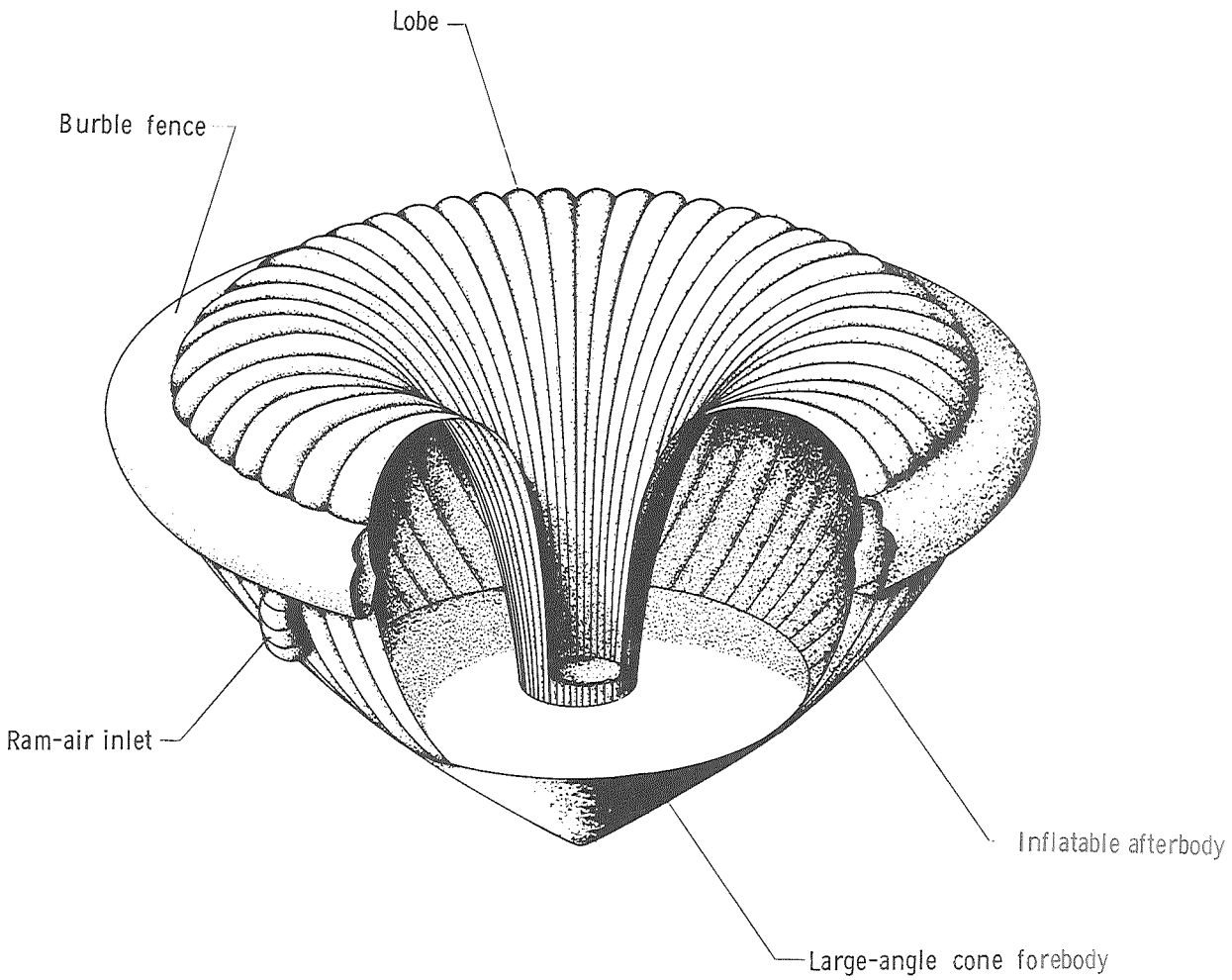

Figure 1.- Illustration of an attached inflatable decelerator.

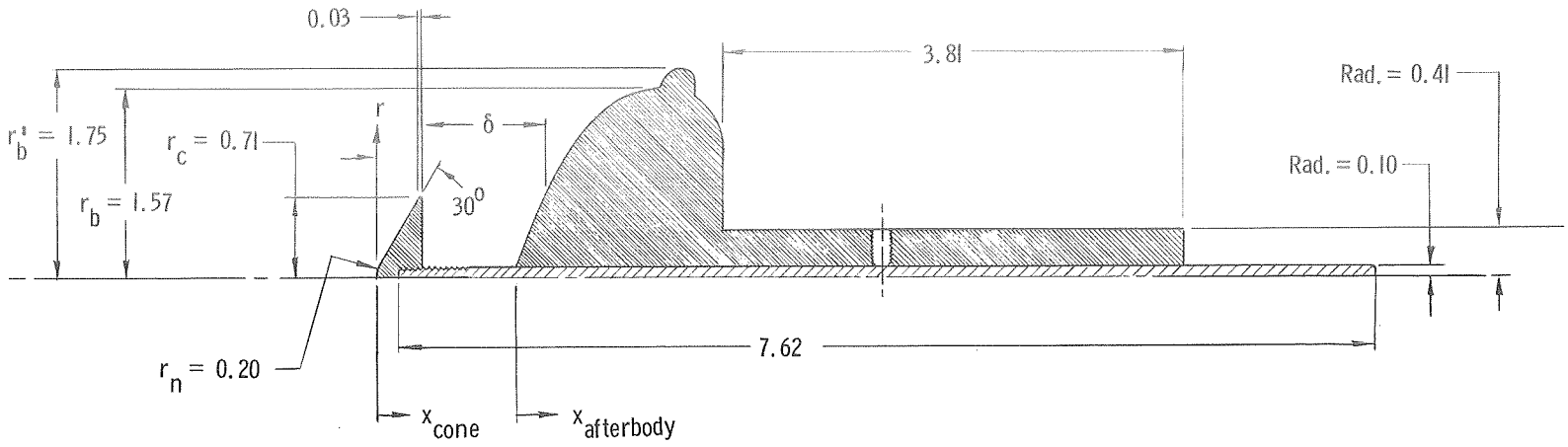

(a) Flow-visualization model.

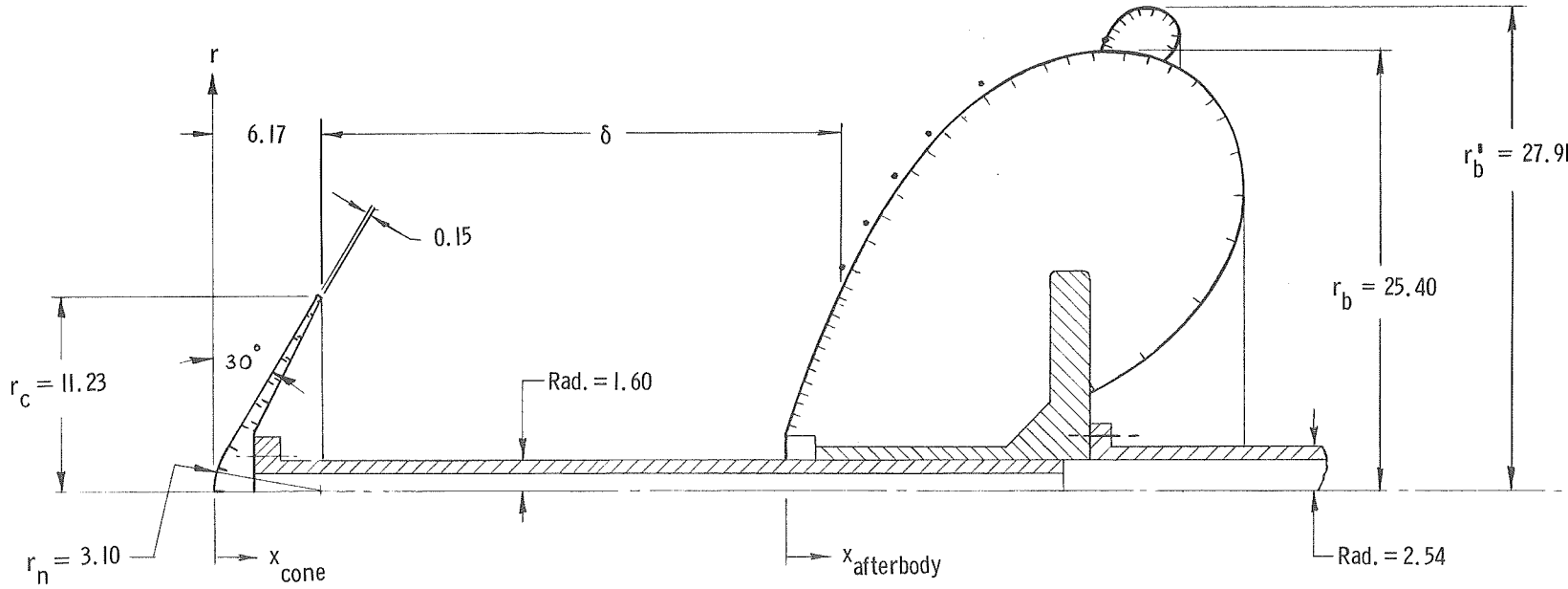

(b) Pressure-distribution model. Dots denote ram-pressure orifices.

Figure 2.- Details of models. Linear dimensions are in centimeters.

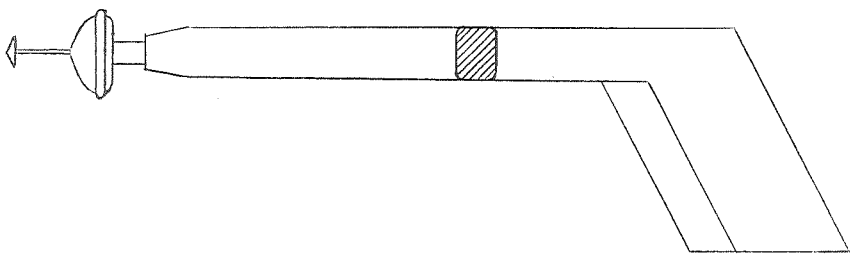

(a) Flow-visualization model and support.

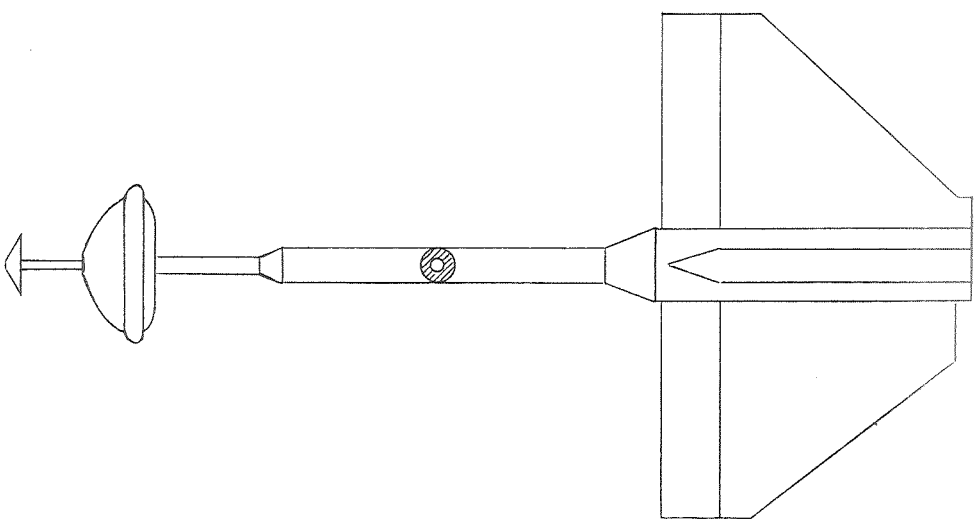

(b) Pressure-distribution model and support.

Figure 3.- Model-sting-mount configurations.

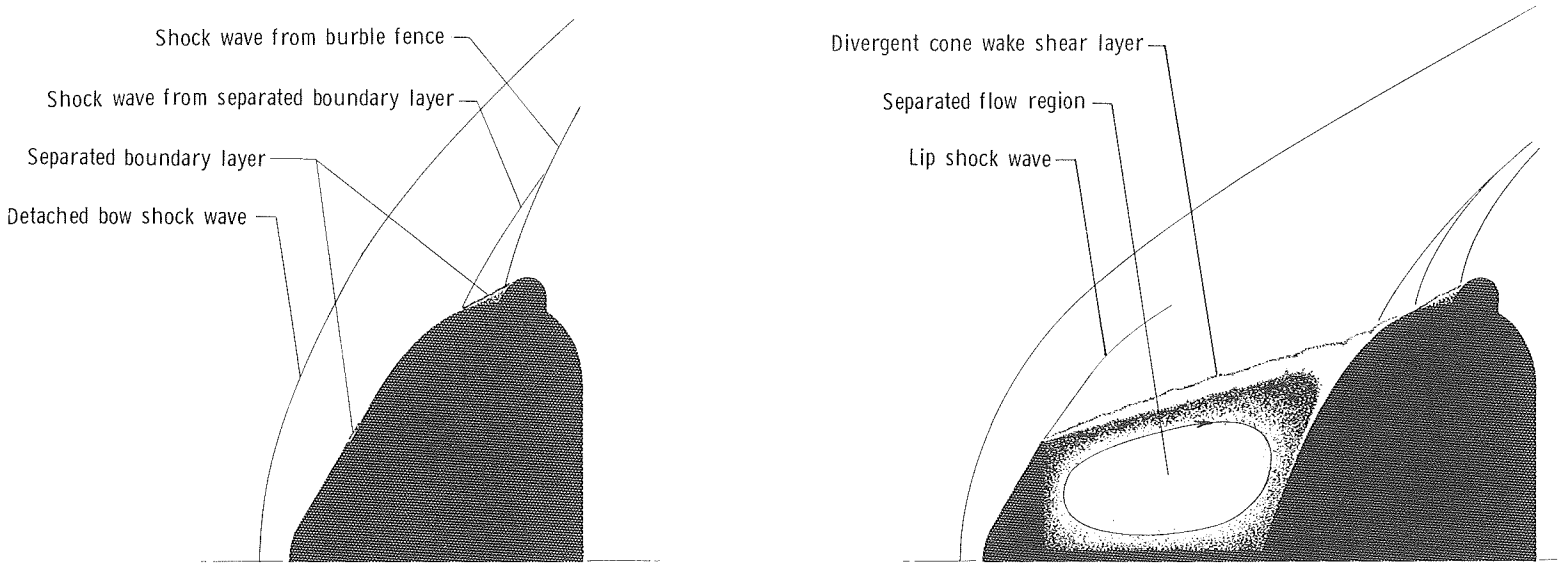

(a) $\frac{\delta}{d_c} = 0.$ (b) $\frac{\delta}{d_c} < 4.60.$

Figure 4.- Typical flow patterns obtained at various separation distances.

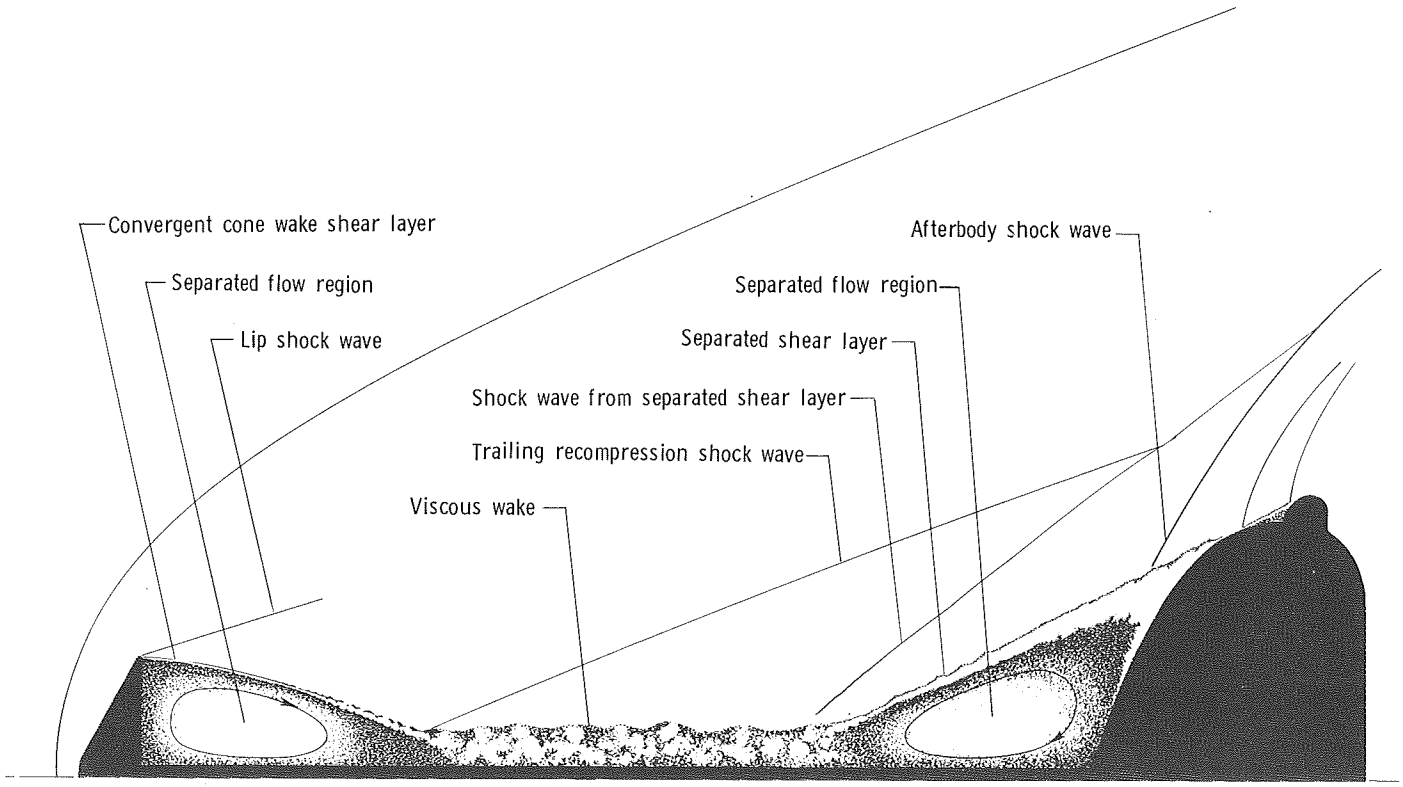

(c) $\frac{\delta}{d_c} > 4.60$.

Figure 4.- Concluded.

L-71-566

Figure 5.- Schlieren photograph of 120° cone at Mach 3.0.

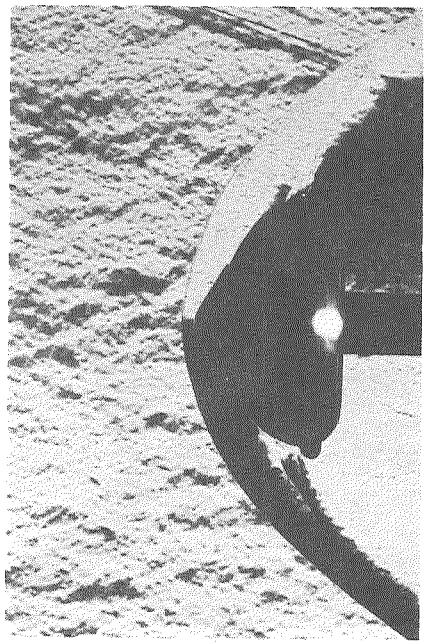

(a) $\frac{\delta}{d_c} = 0.$

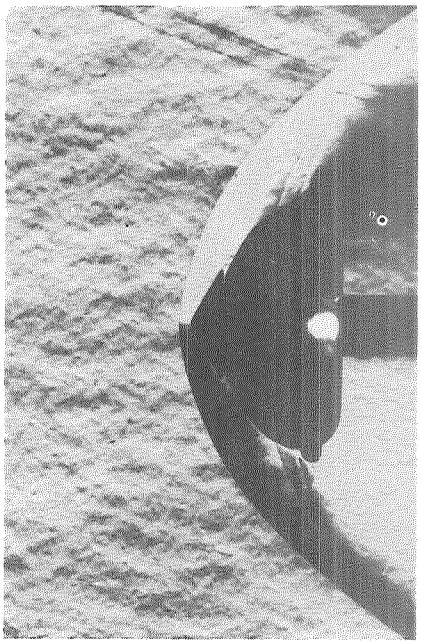

(b) $\frac{\delta}{d_c} = 0.08.$

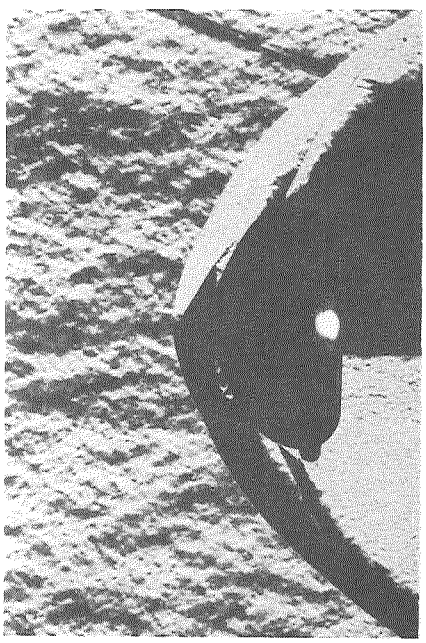

(c) $\frac{\delta}{d_c} = 0.11.$

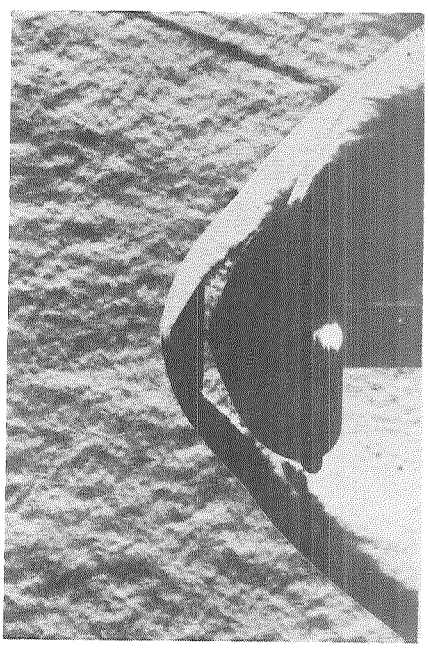

(d) $\frac{\delta}{d_c} = 0.23.$

L-71-567

Figure 6.- Schlieren photographs of decelerator shape showing flow patterns obtained at various separation distances between the 120° cone forebody and the afterbody at Mach 3.0.

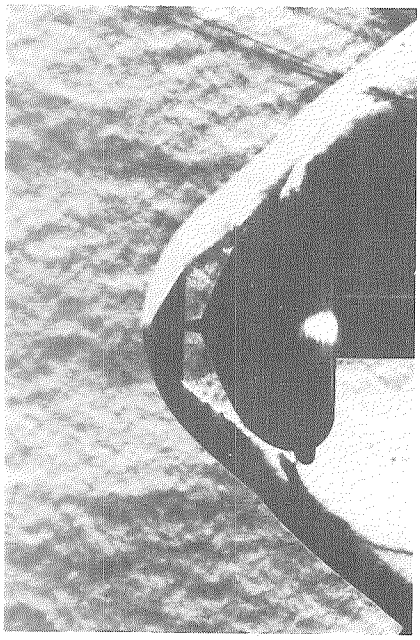

(e) $\frac{\delta}{d_c} = 0.30.$

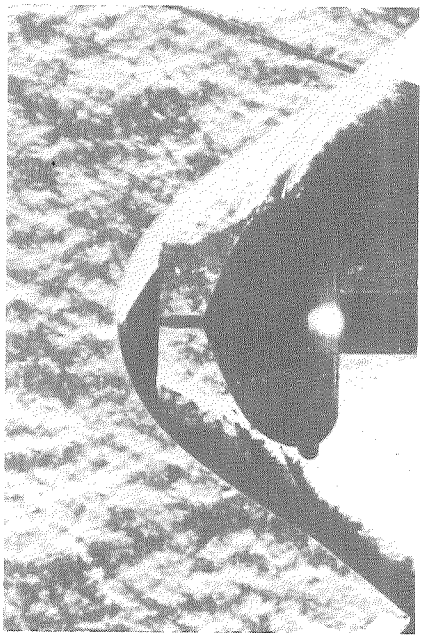

(f) $\frac{\delta}{d_c} = 0.56.$

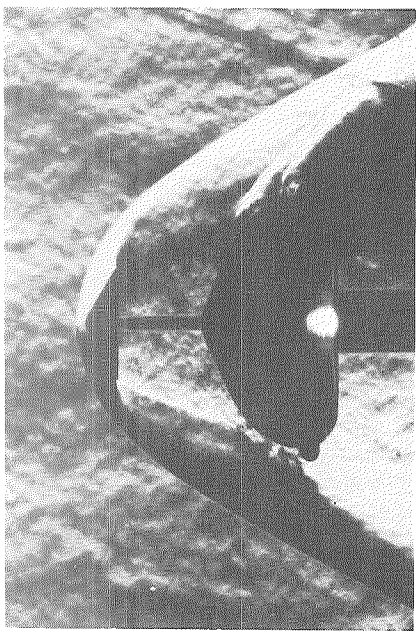

(g) $\frac{\delta}{d_c} = 0.86.$

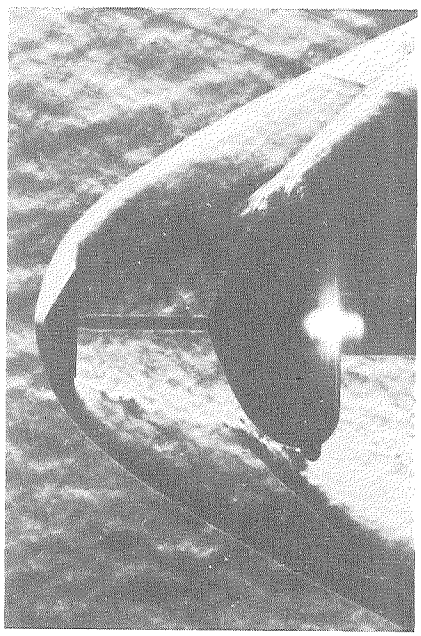

(h) $\frac{\delta}{d_c} = 1.33.$

L-71-568

Figure 6.- Continued.

L-71-569

(i) $\frac{\delta}{d_c} = 2.55.$

Figure 6.- Continued.

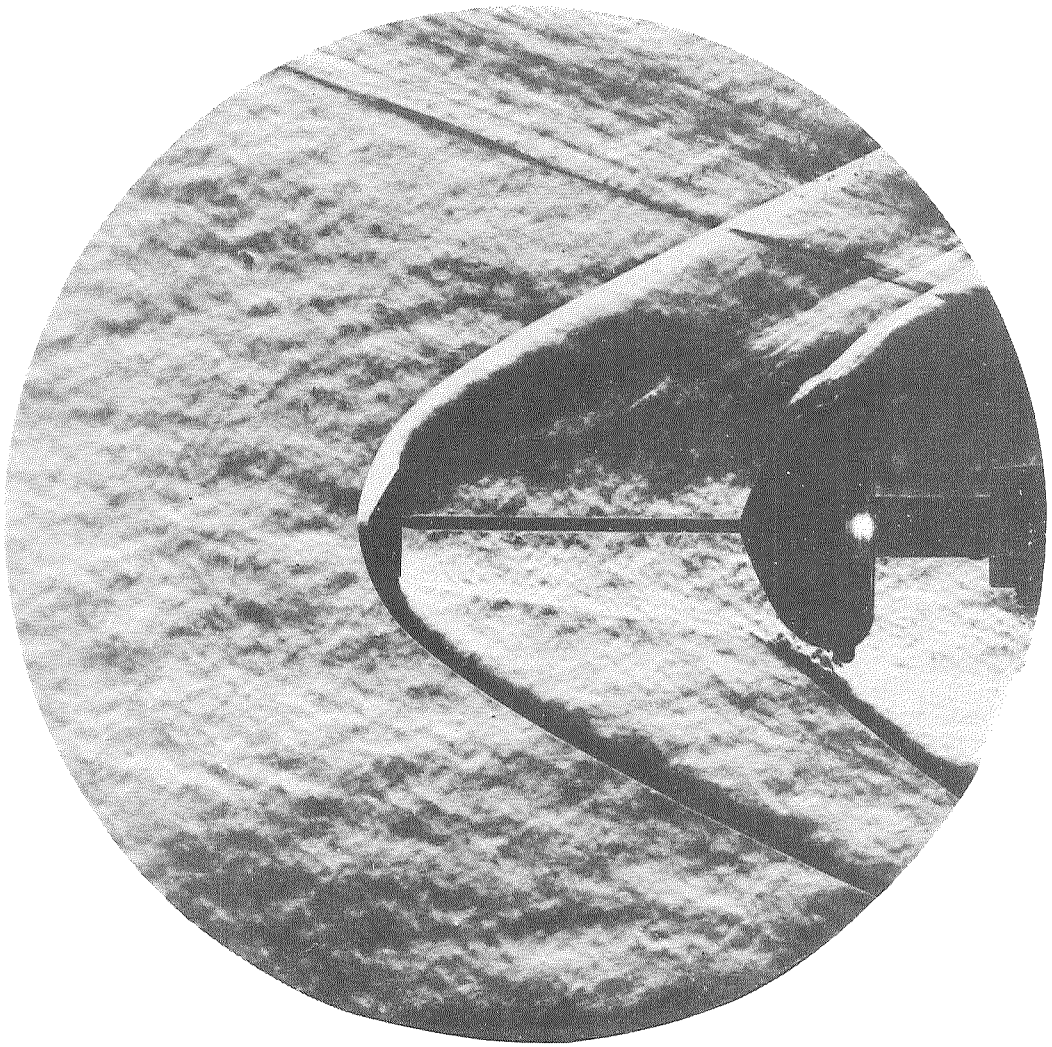

L-71-570

(j) $\frac{\delta}{d_c} = 3.28.$

Figure 6.- Continued.

L-71-571

(k) $\frac{\delta}{d_c} = 4.05.$

Figure 6.- Continued.

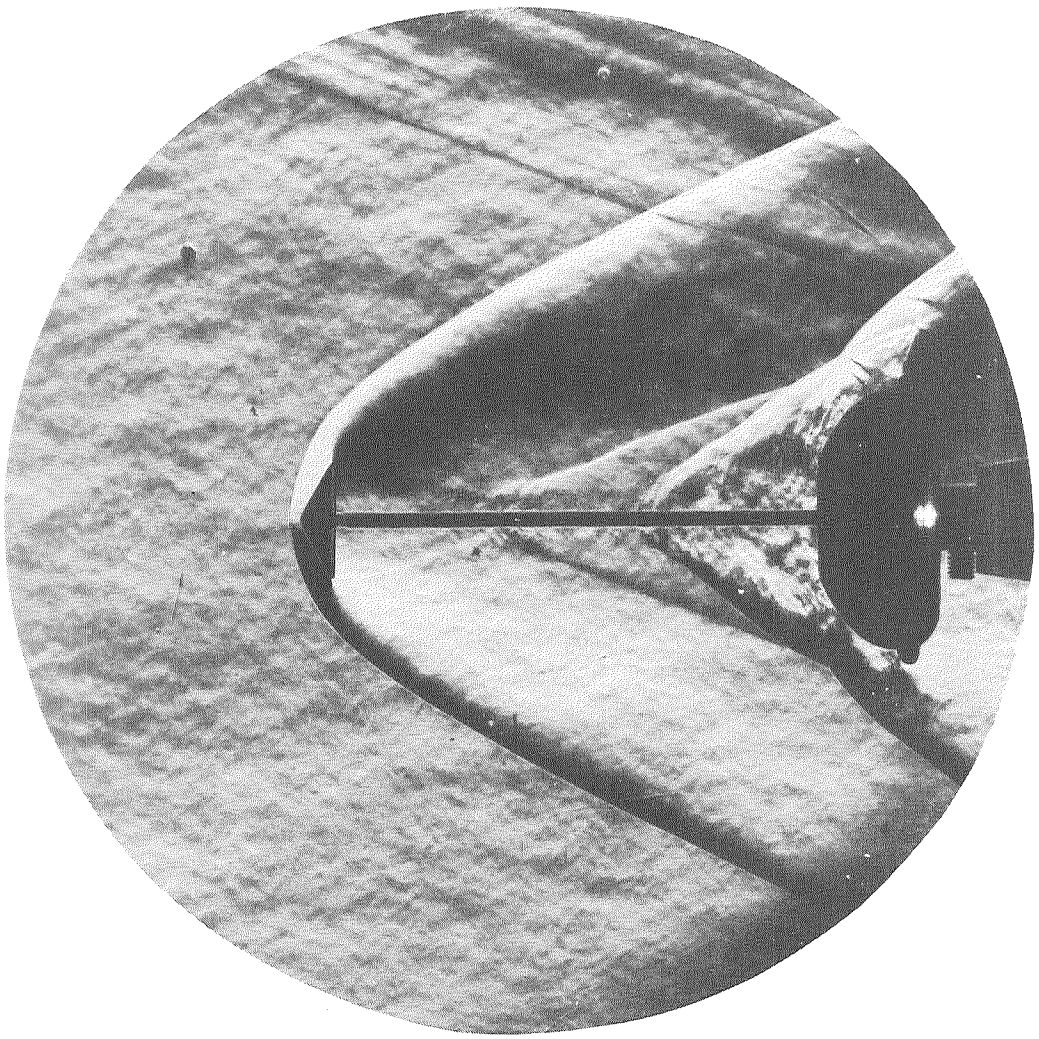

L-71-572

(l) $\frac{\delta}{d_c} = 4.05$.

Figure 6.- Continued.

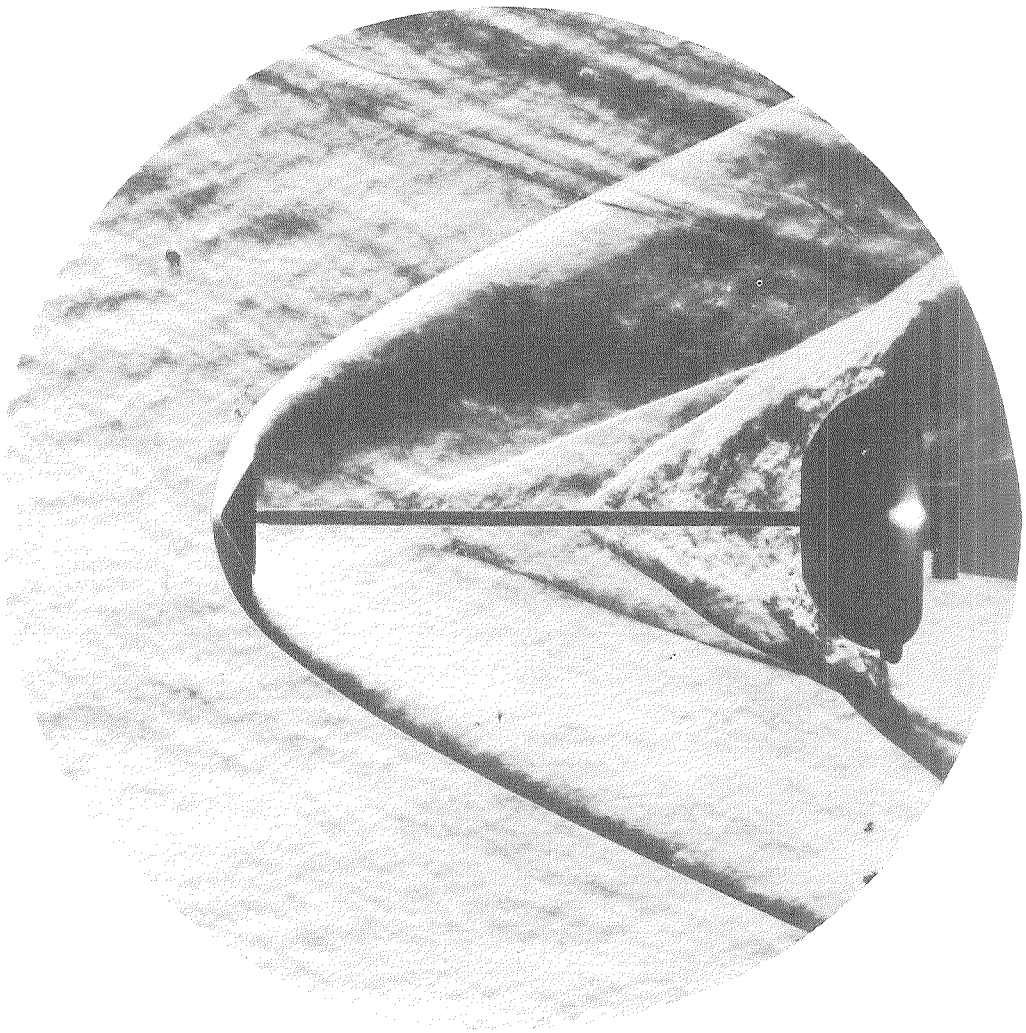

L-71-573

(m) $\frac{\delta}{d_c} = 4.74.$

Figure 6.- Concluded.

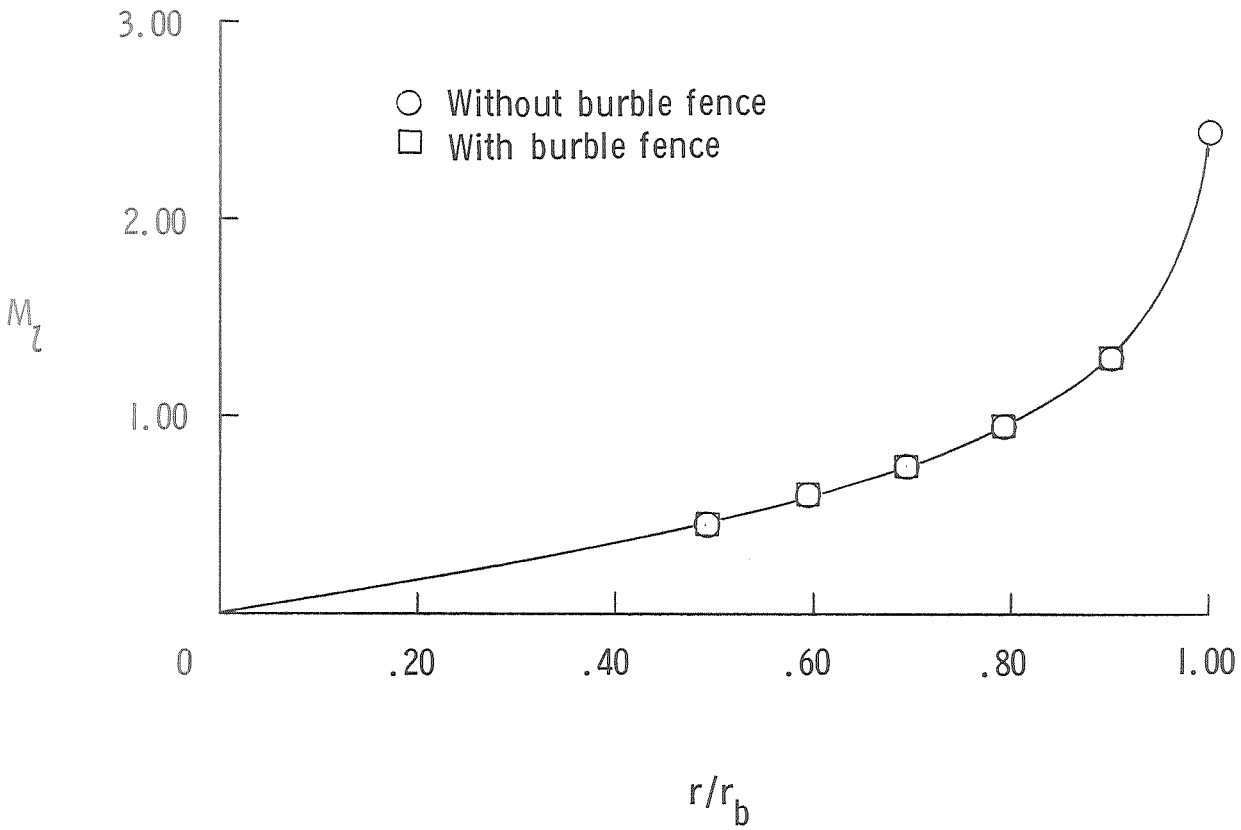

Figure 7.- Surface Mach numbers along decelerator afterbody at zero separation distance for free-stream Mach number of 3.0.

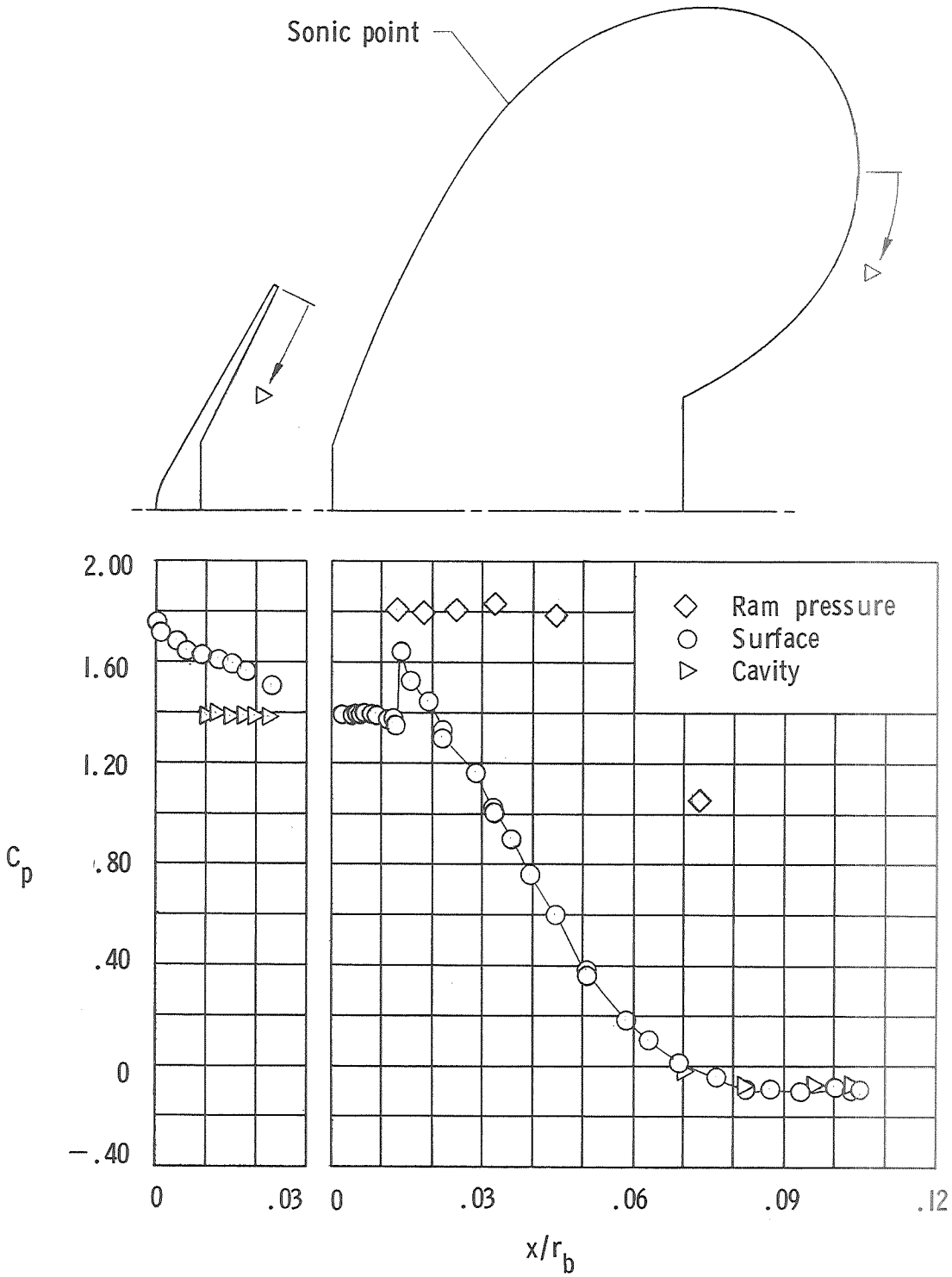

(a) Without burble fence.

Figure 8.- Experimentally determined pressures for $\frac{\delta}{d_c} = 0$.

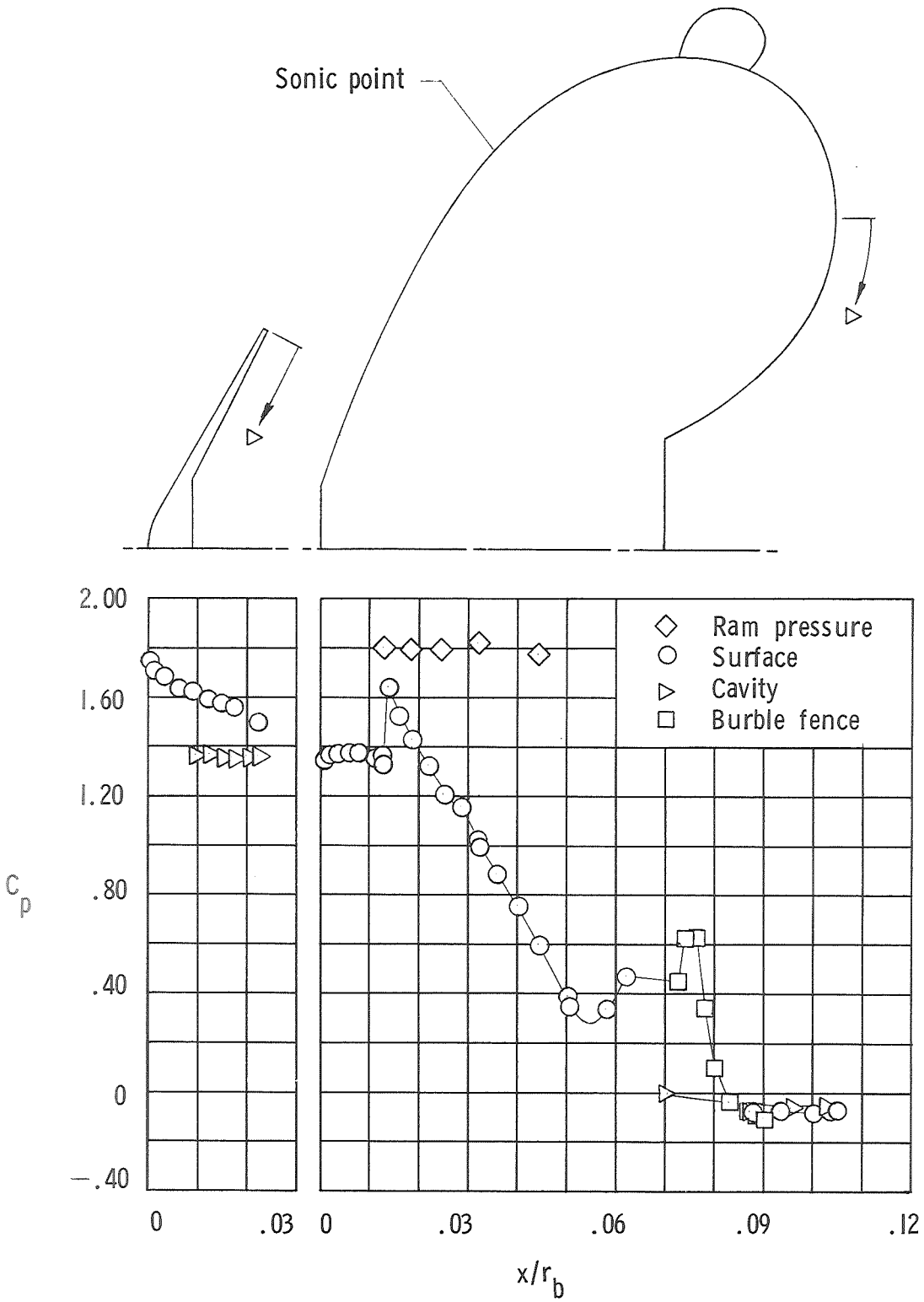

(b) With burble fence.

Figure 8.- Concluded.

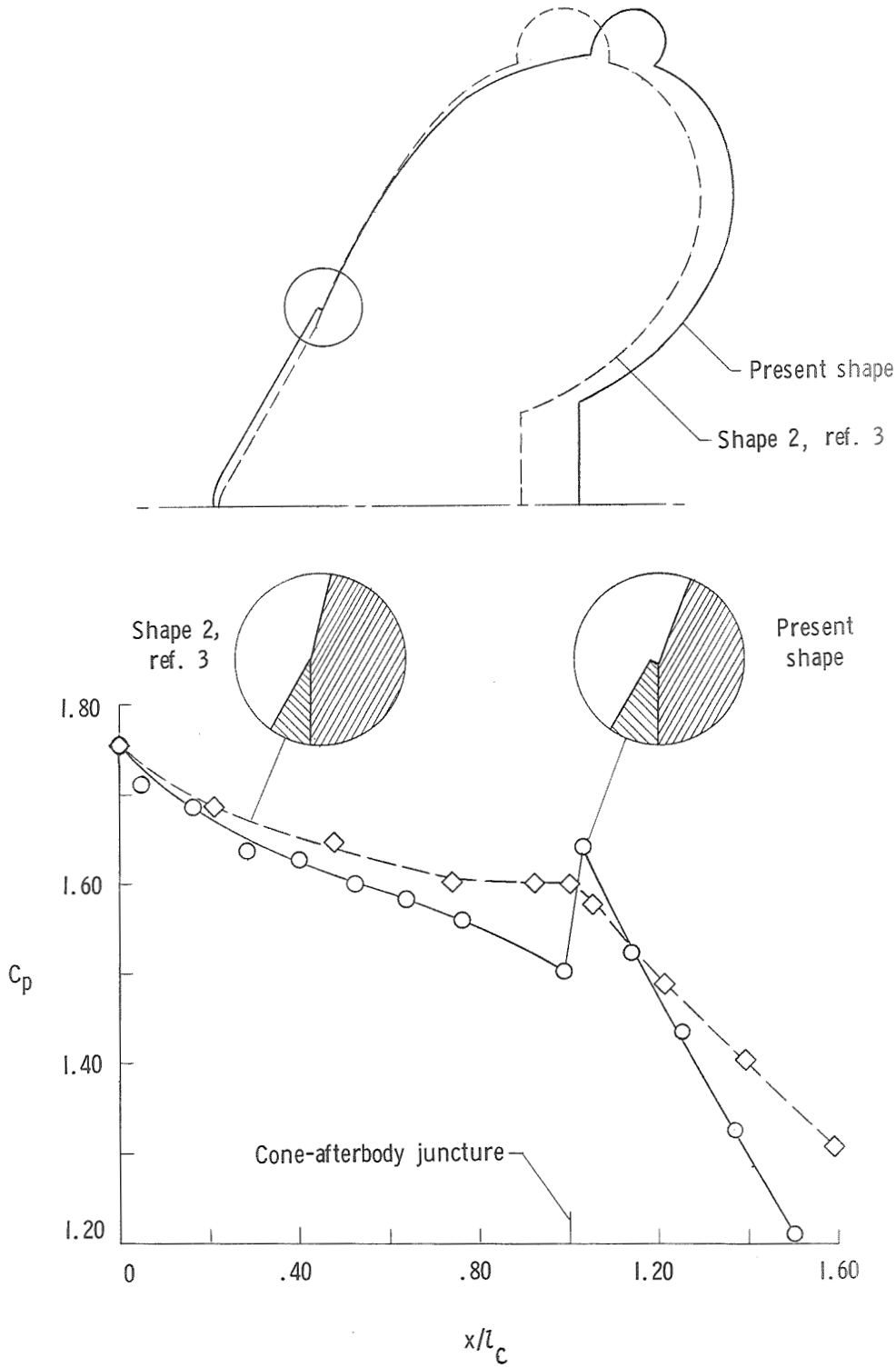

Figure 9.- Effect of cone-afterbody juncture configuration on pressure distribution at Mach 3.0.

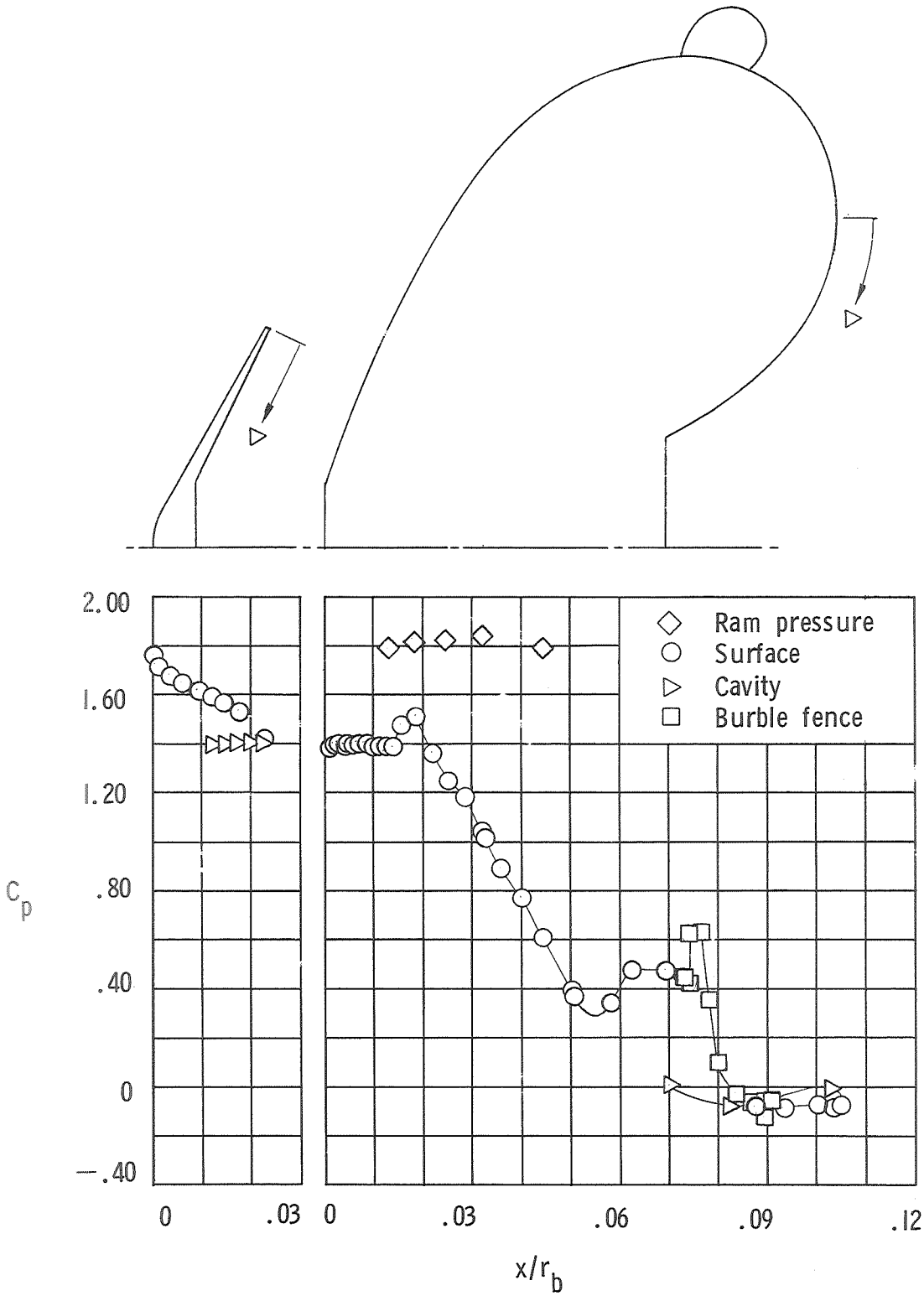

(a) $\frac{\delta}{d_c} = 0.03$.

Figure 10.- Experimentally determined pressures for $\frac{\delta}{d_c} > 0$.

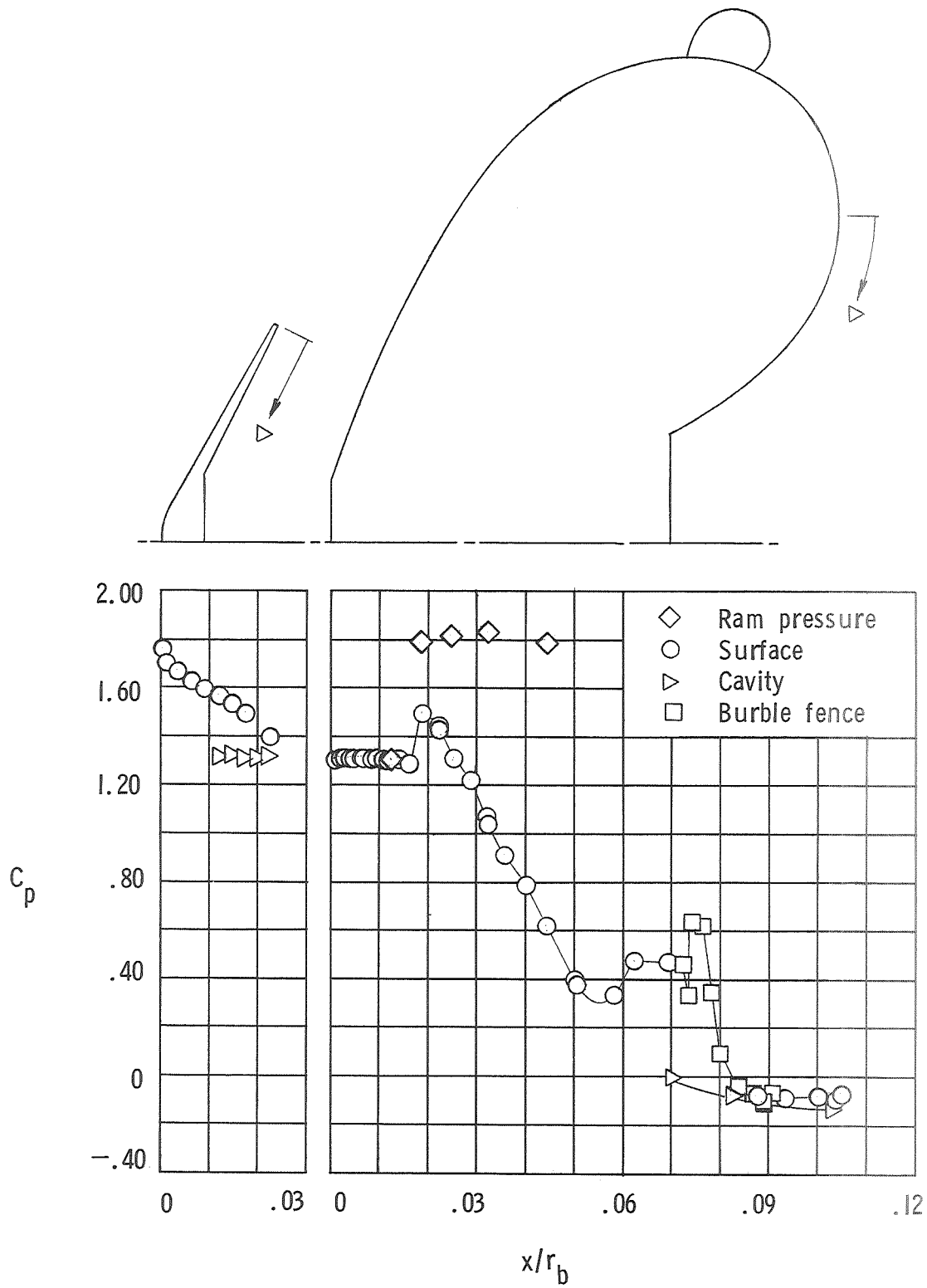

(b) $\frac{\delta}{d_c} = 0.06$.

Figure 10.- Continued.

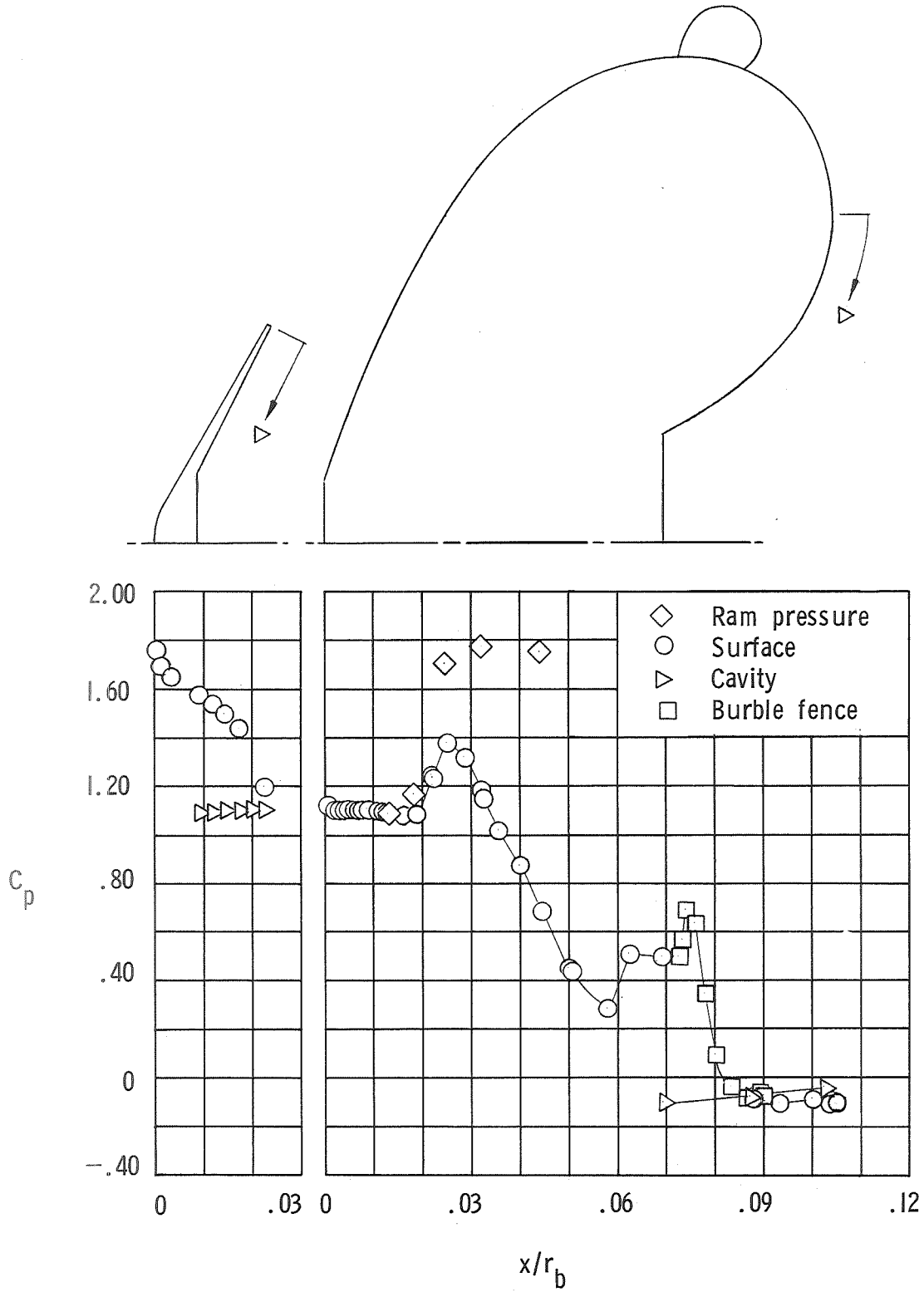

(c) $\frac{\delta}{d_c} = 0.11$.

Figure 10.- Continued.

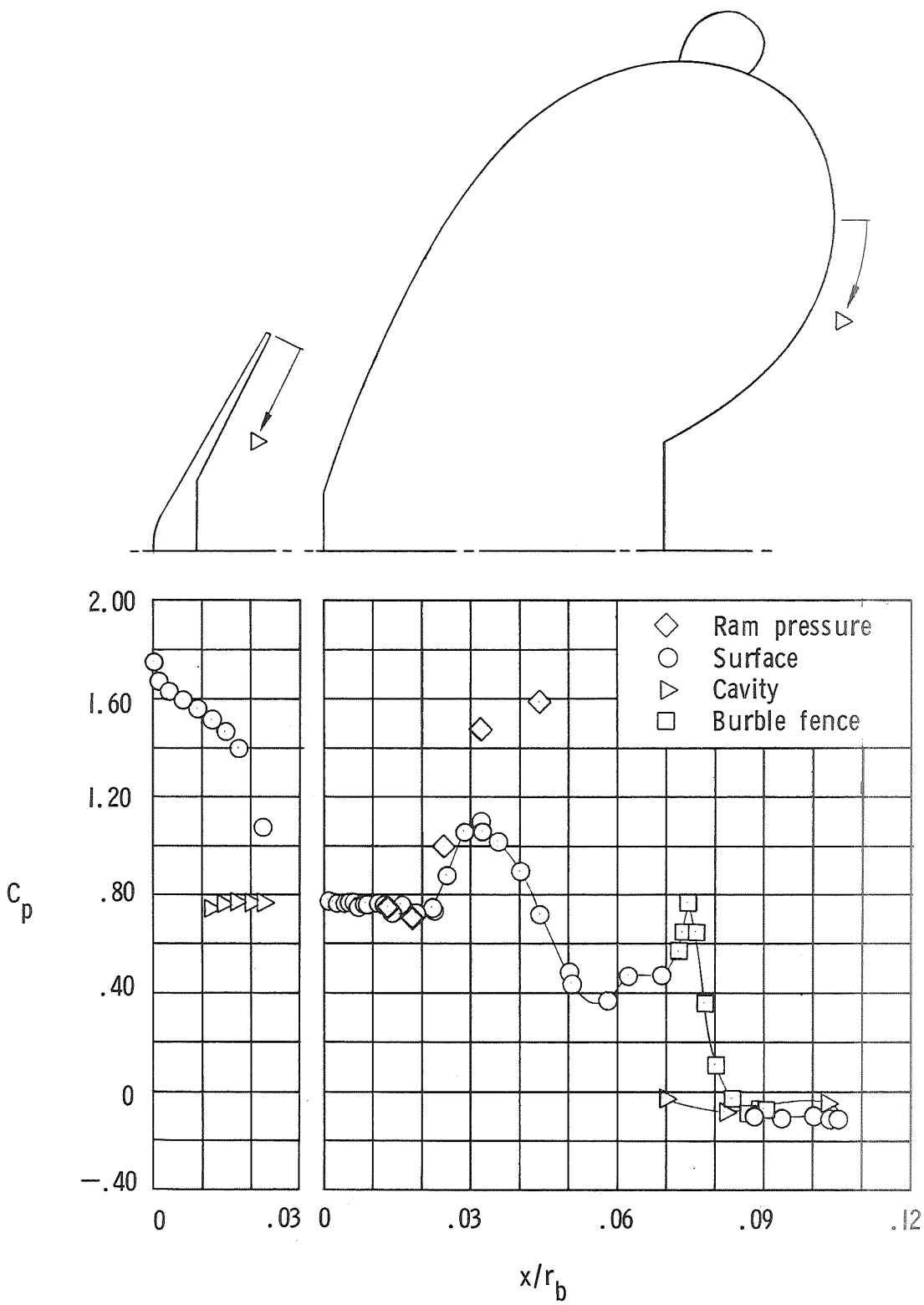

(d) $\frac{\delta}{d_c} = 0.23$.

Figure 10.- Continued.

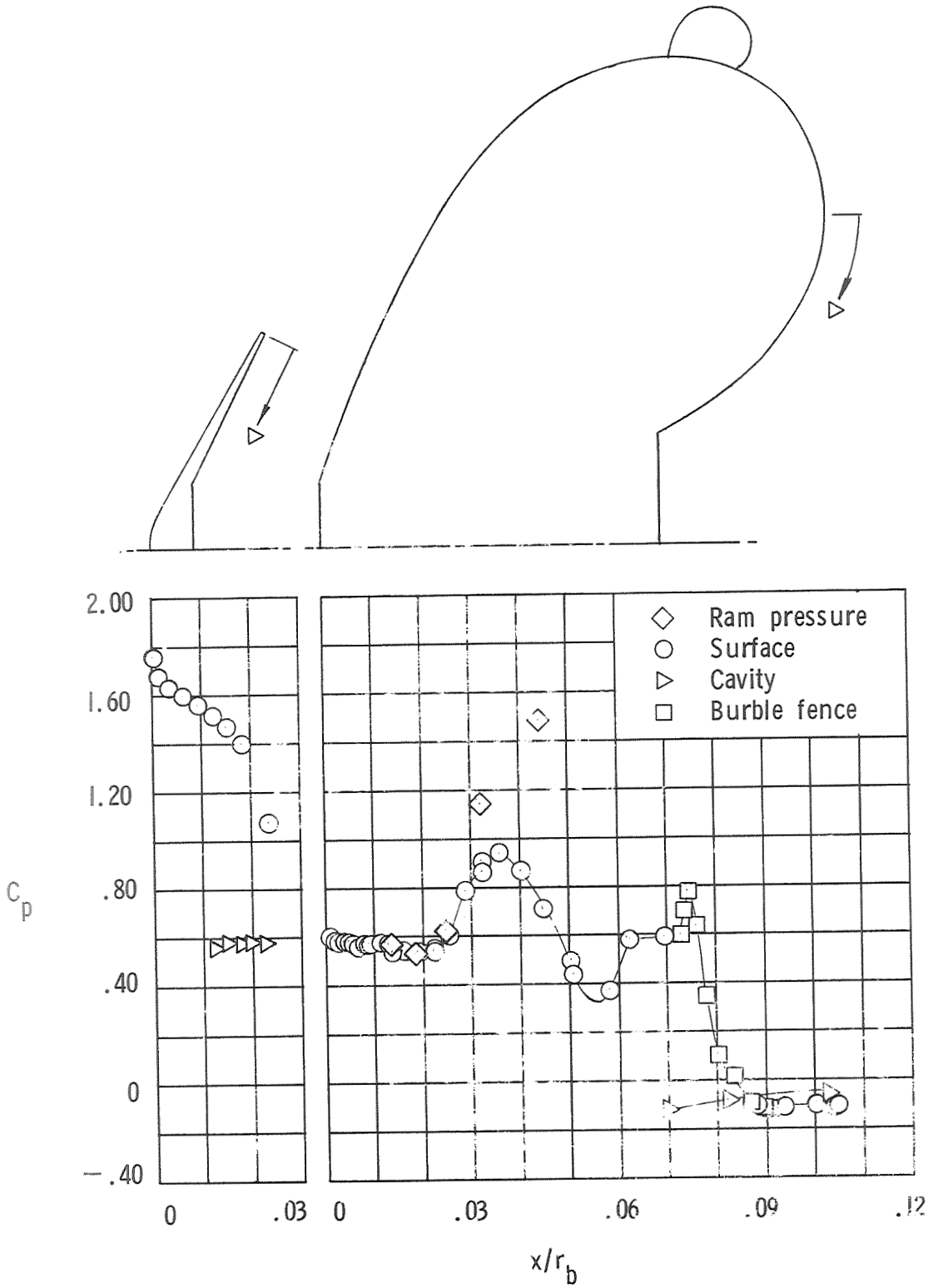

(e) $\frac{\delta}{d_c} = 0.34$.

Figure 10.- Continued.

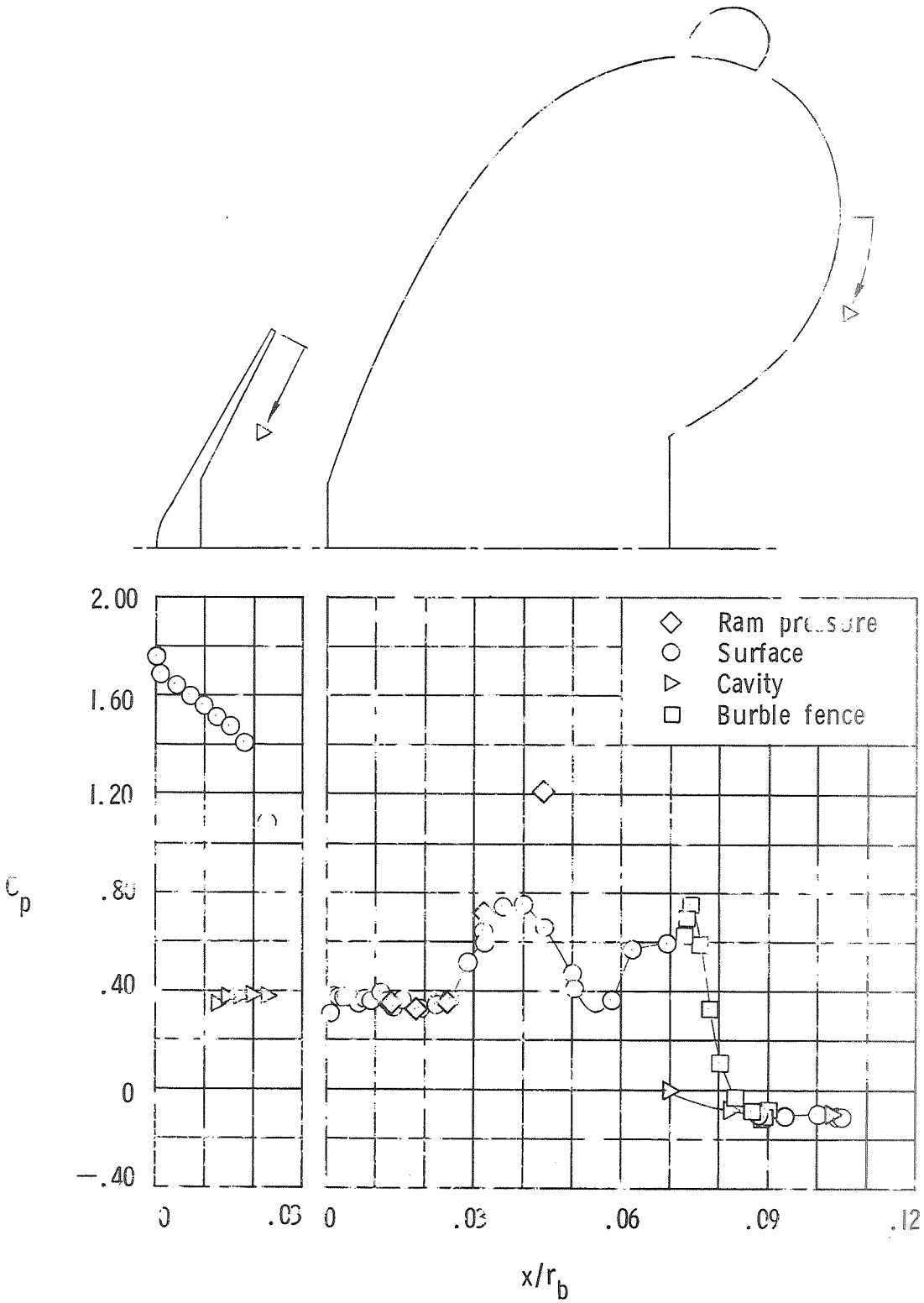

(f) $\frac{\delta}{a_e} = 0.57$.

Figure 10.- Continued.

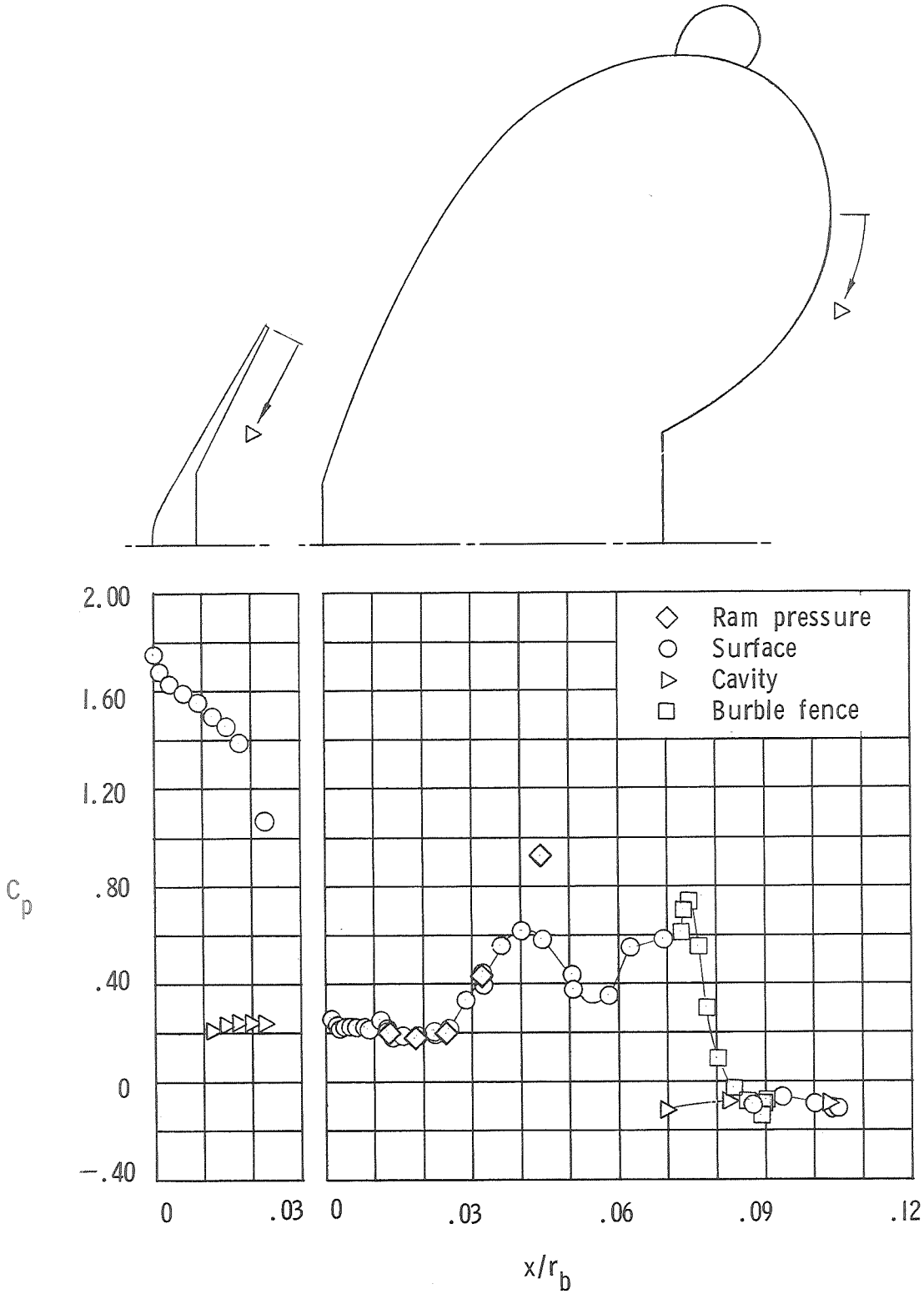

(g) $\frac{\delta}{d_c} = 0.91$.

Figure 10.- Continued.

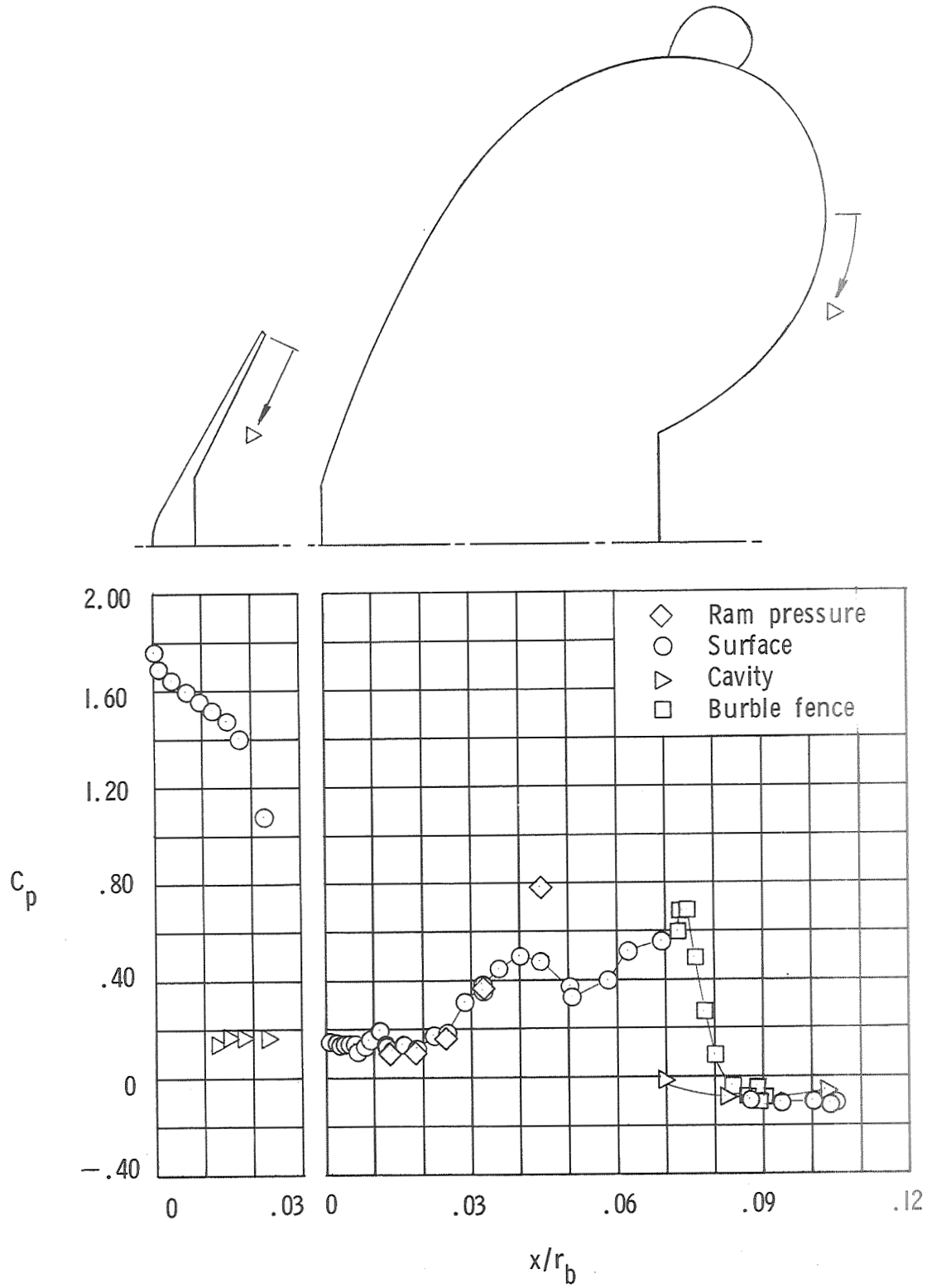

(h) $\frac{\delta}{d_c} = 1.36.$

Figure 10.- Continued.

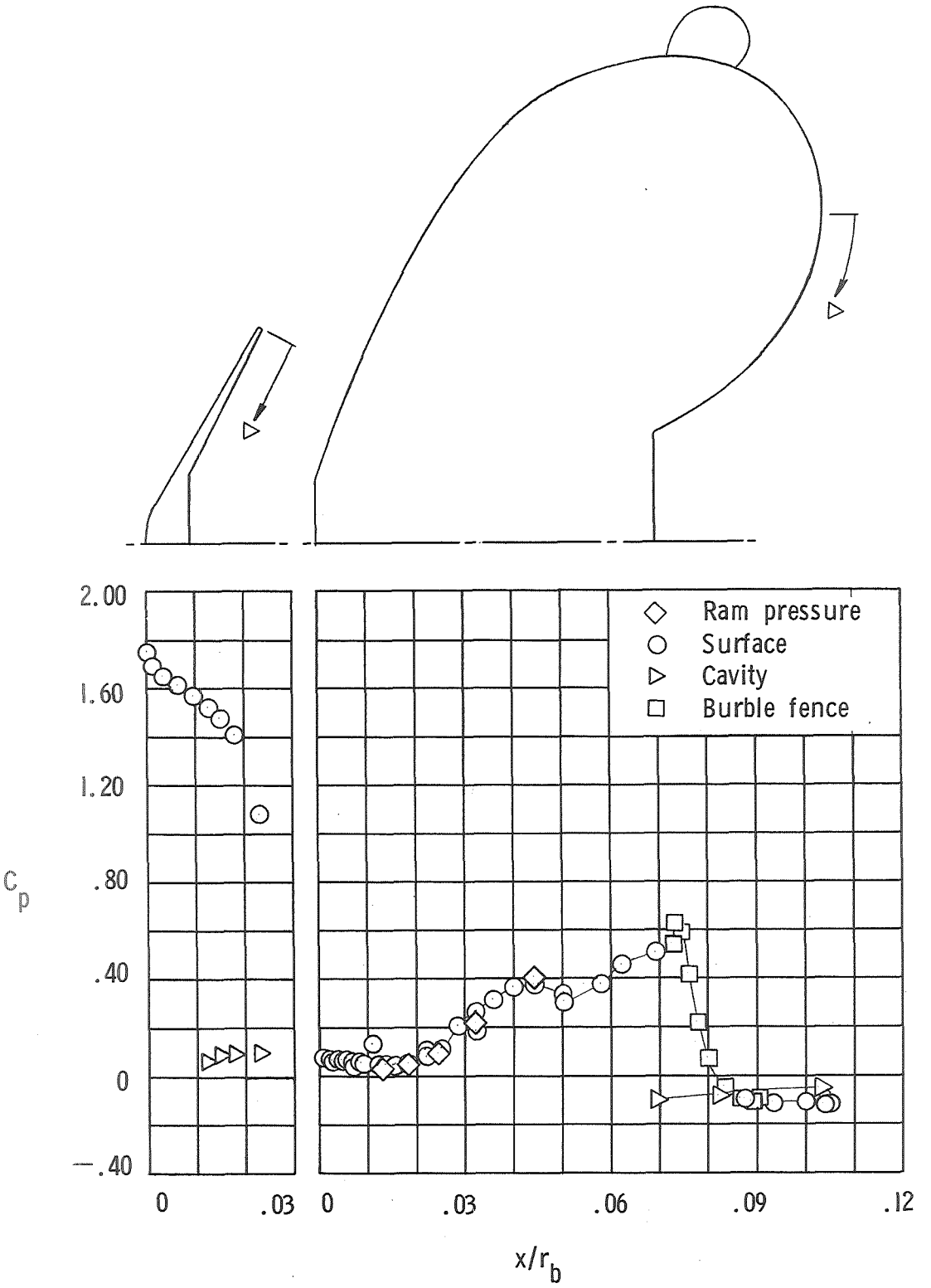

(i) $\frac{\delta}{d_c} = 2.49.$

Figure 10.- Continued.

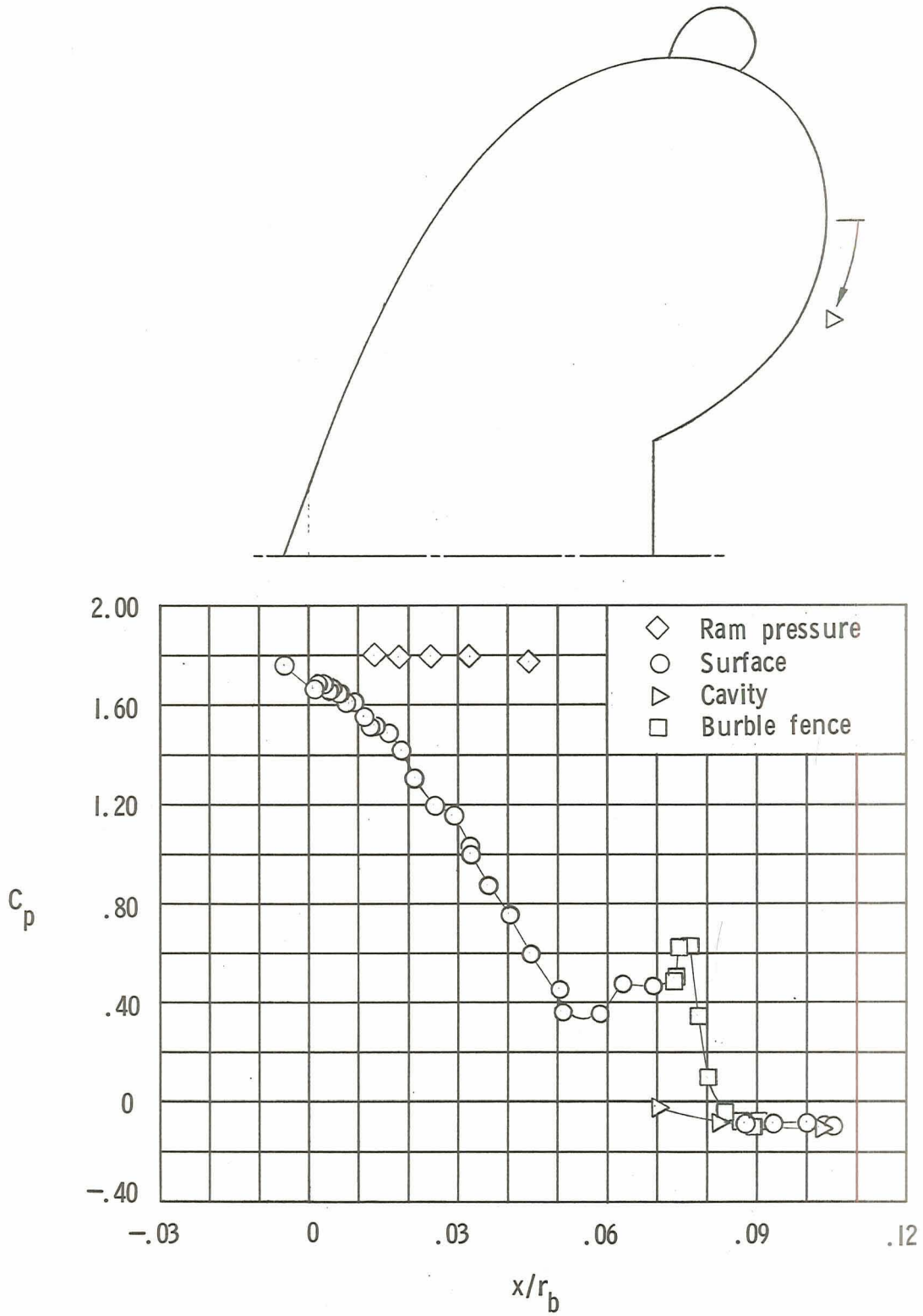

(j) $\frac{\delta}{d_c} = \infty$.

Figure 10.- Concluded.

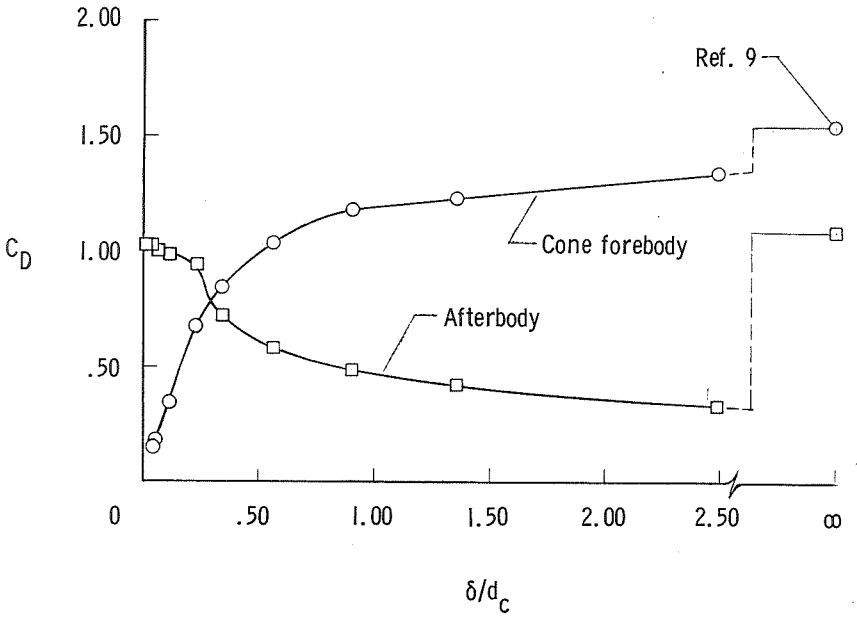

Figure 11.- Variation of forebody and afterbody drag coefficient with body separation distance for a ratio of afterbody to forebody area of 6.2 and for Mach 3.0.

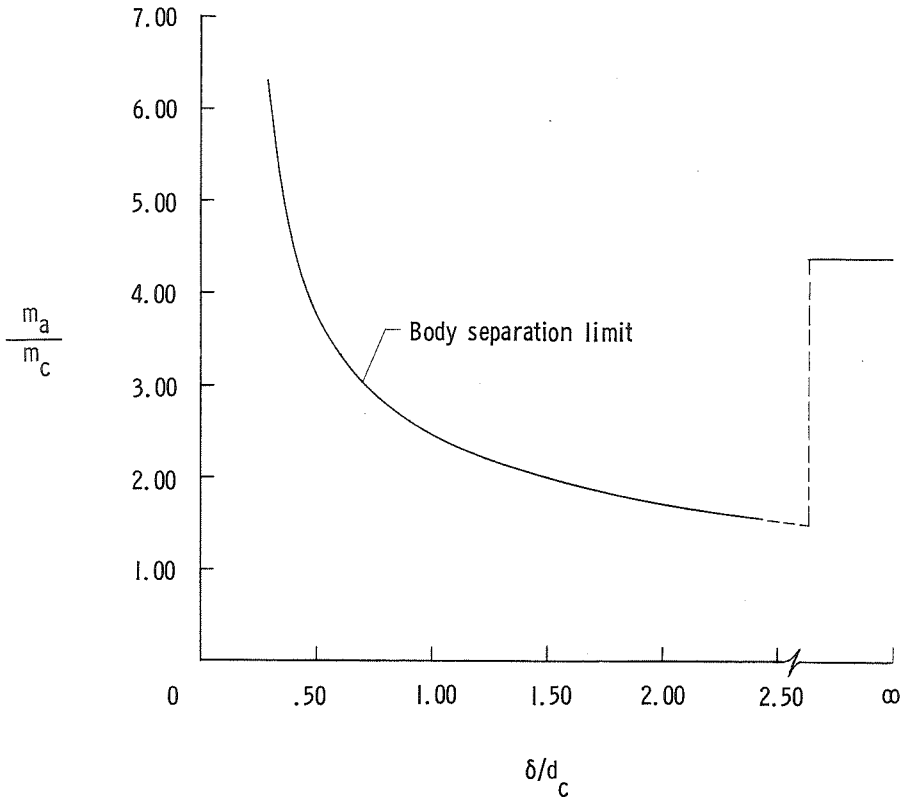

Figure 12.- Variation of afterbody-to-forebody mass ratio with body separation distance for afterbody-to-forebody area ratio of 6.2 and for Mach 3.0.

NASA-Langley, 1971 — 1 L-7542

NATIONAL AERONAUTICS AND SPACE ADMINISTRATION
WASHINGTON, D. C. 20546

OFFICIAL BUSINESS
PENALTY FOR PRIVATE USE $300

FIRST CLASS MAIL

POSTAGE AND FEES PAID
NATIONAL AERONAUTICS AND
SPACE ADMINISTRATION

POSTMASTER: If Undeliverable (Section 158 Postal Manual) Do Not Return

"The aeronautical and space activities of the United States shall be conducted so as to contribute . . . to the expansion of human knowledge of phenomena in the atmosphere and space. The Administration shall provide for the widest practicable and appropriate dissemination of information concerning its activities and the results thereof."

—NATIONAL AERONAUTICS AND SPACE ACT OF 1958

NASA SCIENTIFIC AND TECHNICAL PUBLICATIONS

TECHNICAL REPORTS: Scientific and technical information considered important, complete, and a lasting contribution to existing knowledge.

TECHNICAL NOTES: Information less broad in scope but nevertheless of importance as a contribution to existing knowledge.

TECHNICAL MEMORANDUMS: Information receiving limited distribution because of preliminary data, security classification, or other reasons.

CONTRACTOR REPORTS: Scientific and technical information generated under a NASA contract or grant and considered an important contribution to existing knowledge.

TECHNICAL TRANSLATIONS: Information published in a foreign language considered to merit NASA distribution in English.

SPECIAL PUBLICATIONS: Information derived from or of value to NASA activities. Publications include conference proceedings, monographs, data compilations, handbooks, sourcebooks, and special bibliographies.

TECHNOLOGY UTILIZATION PUBLICATIONS: Information on technology used by NASA that may be of particular interest in commercial and other non-aerospace applications. Publications include Tech Briefs, Technology Utilization Reports and Technology Surveys.

Details on the availability of these publications may be obtained from:

SCIENTIFIC AND TECHNICAL INFORMATION OFFICE

NATIONAL AERONAUTICS AND SPACE ADMINISTRATION

Washington, D.C. 20546